Mon. Not. R. Astron. Soc. **348,** 753–782 (2004) doi:10.1111/j.1365-2966.2004.07364.x

Photoevaporation of cosmological minihaloes during reionization

Paul R. Shapiro,[1]★ Ilian T. Iliev[2]† and Alejandro C. Raga[3]

[1]*Department of Astronomy, University of Texas, Austin, TX 78712-1083, USA*
[2]*Osservatorio Astrofisico di Arcetri, Largo Enrico Fermi 5, 50125 Firenze, Italy*
[3]*Instituto de Ciencias Nucleares, Universidad Nacional Autonoma de México (UNAM), Apdo. Postal 70-543, 04510 México, DF, México*

Accepted 2003 October 31. Received 2003 October 27; in original form 2003 July 17

ABSTRACT

Energy released by a small fraction of the baryons in the Universe, which condensed out while the intergalactic medium (IGM) was cold, dark and neutral, reheated and reionized it by redshift 6, exposing other baryons already condensed into dwarf-galaxy minihaloes to the glare of ionizing radiation. We present the first gas dynamical simulations of the photoevaporation of cosmological minihaloes overtaken by the ionization fronts which swept through the IGM during the reionization epoch in the currently favoured Λ cold dark matter (ΛCDM) universe, including the effects of radiative transfer. These simulations demonstrate the phenomenon of I-front trapping inside minihaloes, in which the weak, R-type fronts which travelled supersonically across the IGM decelerated when they encountered the dense, neutral gas inside minihaloes, and were thereby transformed into D-type I-fronts, preceded by shock waves. For a minihalo with virial temperature below 10^4 K, the I-front gradually burned its way through the minihalo which trapped it, removing all of its baryonic gas by causing a supersonic, evaporative wind to blow backwards into the IGM, away from the exposed layers of minihalo gas just behind the advancing I-front. We describe this process in detail, along with some of its observable consequences, for the illustrative case of a minihalo of total mass 10^7 $M_\odot$, exposed to a distant source of ionizing radiation with either a stellar or quasar-like spectrum, after it was overtaken at redshift $z = 9$ by the weak, R-type I-front which ionized the IGM surrounding the source. For a source at $z = 9$ which emits 10^{56} ionizing photons per second at 1 Mpc (or, equivalently, 10^{52} ionizing photons per second at 10 kpc), the photoevaporation of this minihalo takes about 100–150 Myr, depending on the source spectrum, ending at about $z = 7.5$.

Such hitherto neglected feedback effects were widespread during the reionization epoch. *N*-body simulations and analytical estimates of halo formation in the ΛCDM model suggest that sub-kpc minihaloes such as these, with virial temperatures below 10^4 K, were so common as to cover the sky around larger-mass source haloes and possibly dominate the absorption of ionizing photons during reionization. This means that previous estimates of the number of ionizing photons per hydrogen atom required to complete reionization which neglected this effect may be too low. Regardless of their effect on the progress of reionization, however, the minihaloes were so abundant that random lines of sight through the high-z Universe should encounter many of them, which suggests that it may be possible to observe the processes described here in the absorption spectra of distant sources.

Key words: hydrodynamics – radiative transfer – galaxies: haloes – galaxies: high-redshift – intergalactic medium – cosmology: theory.

★Email: shapiro@astro.as.utexas.edu
†Present address: Canadian Institute for Theoretical Astrophysics, University of Toronto, 60 St George Street, Toronto, ON M5S 3H8, Canada.

1 INTRODUCTION

1.1 The reionization epoch

Observations of the intergalactic medium (IGM) indicate that the Universe was reionized by redshift $z \approx 6$ but that reionization began long before this. The absence of a Gunn–Peterson (GP) trough in the spectra of high-redshift quasars at observed wavelengths $\lambda_\alpha(1+z)$ due to Lyα resonance scattering by hydrogen atoms in the IGM at $z < 6$ indicates that the IGM was very highly ionized at all $z < 6$ (Fan et al. 2000). Since the Universe recombined at $z \sim 1000$, something must have occurred to reionize it by $z \sim 6$.

The detection of GP troughs in the spectra of Sloan Digital Sky Survey (SDSS) quasars at $z \geqslant 6$ places a lower limit on the mean H I density in the IGM at $z = 6$ large enough to suggest that reionization might only just have ended at $z \approx 6$ (Becker et al. 2001; Djorgovski et al. 2001; Fan et al. 2003). Limits on the GP effect at $z < 6$, that is, imply a hydrogen neutral fraction significantly *smaller* than the value at $z = 6$, which can be explained by a photoionized IGM only if the ionizing background radiation increased dramatically in a short interval of cosmic time at this epoch (Cen & McDonald 2002; Fan et al. 2002). Since reionization is believed to have proceeded inhomogeneously, with isolated patches of ionized gas which eventually grew to fill all of space, the epoch of overlap would have been accompanied by the required rapid increase in the ionizing radiation background, as the absorption mean free path for this radiation suddenly increased. For this reason, the GP detections at $z = 6$ and limits at $z < 6$ are thought to indicate that the epoch of overlap – the end of reionization – occurred at a redshift close to $z = 6$.

The recent discovery by the *WMAP* satellite of polarization of the cosmic microwave background (CMB) which fluctuates on an angular scale of 10°, on the other hand, amounts to a detection of a foreground electron scattering optical depth through the IGM of $\tau_{\rm es} \simeq 0.17 \pm 0.04$ (Kogut et al. 2003; Spergel et al. 2003). This suggests that the IGM was either mostly ionized by a redshift of $z \simeq 17 \pm 5$, or else was at least partially ionized starting at even higher z (Spergel et al. 2003). The GP detection at $z = 6$ described above argues against the simplest interpretation of the *WMAP* polarization result in which the Universe was fully reionized by redshift $z \gtrsim 15$ and stayed ionized thereafter. Another argument against that simple interpretation is based upon the fact that, after the IGM was reheated by its reionization, it would gradually have cooled by adiabatic expansion even though it continued to be photoionized by background radiation. If reionization finished as early as implied by the simplest interpretation of the *WMAP* results, this would have lowered the temperature of the IGM at redshifts $z \leqslant 4$ below the level deduced from the Ly α forest (Hui & Haiman 2003).

In short, reionization is currently believed to have begun by redshift $z \gtrsim 15$ to accommodate the *WMAP* results but to extend until $z = 6$ to accommodate observations of the GP effect and of the Ly α forest at $z \leqslant 6$. When and how this reionization occurred and what its consequences were for the subsequent epochs is one of the major unsolved problems of cosmology.

1.2 Ionization fronts in the IGM

The neutral, opaque IGM out of which the first bound objects condensed was dramatically reheated and reionized at some time between a redshift $z \approx 30$ and $z \approx 6$ by the radiation released by some of these objects. When the first sources turned on, they ionized their surroundings by propagating weak, R-type ionization fronts which moved outward supersonically with respect to both the neutral gas ahead of and the ionized gas behind the front, racing ahead of the hydrodynamical response of the IGM, as first described by Shapiro (1986) and Shapiro & Giroux (1987). These authors solved the problem of the time-varying radius of a spherical I-front which surrounds an isolated source in a cosmologically expanding IGM analytically, generalizing the I-front jump condition and radiative transfer to cosmological conditions. They applied these solutions to determine when and how fast the I-fronts surrounding isolated sources would grow to overlap and, thereby, complete the reionization of the Universe.[1] The effect of density inhomogeneity on the rate of the I-front propagation was described by a mean 'clumping factor' $C \equiv \langle n^2 \rangle / \langle n \rangle^2 > 1$, which slowed the I-fronts by increasing the average recombination rate per atom inside clumps. This suffices to describe the rate of I-front propagation as long as the clumps are either not self-shielding or, if so, only absorb a small fraction of the ionizing photons emitted by the central source.

Numerical radiative transfer methods are currently under development to solve this problem in 3D for the inhomogeneous density distribution which arises as cosmic structure forms, so far primarily limited to the transfer of ionizing radiation through pre-computed density fields generated by cosmological simulations which do not include radiative transfer, so there is no back-reaction of the radiative transfer calculation on the density field or any aspect of the gas dynamics (Abel, Norman & Madau 1999; Razoumov & Scott 1999; Ciardi et al. 2001; Nakamoto, Umemura & Susa 2001; Sokasian, Abel & Hernquist 2001; Cen 2002; Ciardi, Stoehr & White; Hayes & Norman 2003). Approximate approaches which incorporate some of the important effects of radiative transport during reionization within the context of cosmological gas dynamics simulation have also been developed (Gnedin 2000a; Gnedin & Abel 2001; Ricotti, Gnedin & Shull 2002a). These recent attempts to model inhomogeneous reionization numerically are generally handicapped by their limited spatial resolution, which prevents them from fully resolving the most important (sub-kpc-sized) density inhomogeneities. The questions of what dynamical effect the I-front had on the density inhomogeneities it encountered and how the presence of these inhomogeneities affected the I-fronts and reionization, therefore, require further analysis.

Towards this end, we have developed a radiation-hydrodynamics code which incorporates radiative transfer and focused our attention on properly resolving this small-scale structure. Here we shall present in some detail our results of the first radiation-hydrodynamical simulations of the back-reaction of a cosmological I-front on a gravitationally bound density inhomogeneity it encounters – a 10^7 $M_\odot$ dwarf-galaxy minihalo – during reionization, along with some general considerations which apply to other haloes as well. A second paper to follow will present the results for a much wider range of cases, with different halo masses and I-front encounter epochs, to quantify just how the process described here varies with these properties. As it turns out, the photoevaporation of sub-kpc-sized objects like these may be the dominant process by which ionizing photons are absorbed during reionization, so this problem is of critical importance. In addition, observations of the absorption spectra of high-redshift sources like those which reionized

[1] This provided the first indication that quasars alone did not reionize the Universe; the observed quasar luminosity function extrapolated to higher redshift was not sufficient to do so in time to satisfy the GP constraint, suggesting that some other source was responsible, such as starlight.

the Universe should reveal the presence of these photoevaporative flows and provide a useful diagnostic of the reionization process.

1.3 The photoevaporation of dwarf-galaxy minihaloes overtaken by cosmological ionization fronts

The effect which small-scale clumpiness had on reionization depended upon the sizes, densities, and spatial distribution of the clumps overtaken by the I-fronts during reionization. For the currently favoured ΛCDM model ($\Omega_0 = 1 - \lambda_0 = 0.3, h = 0.7, \Omega_b h^2 = 0.02$, primordial power spectrum index $n_p = 1$; *COBE*-normalized), which is the model we adopt throughout this paper, the Universe at $z > 6$ was already filled with dwarf galaxies capable of trapping some of the global, intergalactic I-fronts which reionized the Universe and photoevaporating their gaseous baryons back into the IGM. Prior to their encounter with these I-fronts, 'minihaloes' with $T_{\rm vir} \leqslant 10^4$ K were neutral and optically thick to hydrogen ionizing radiation, as long as their total mass exceeded the Jeans mass M_J in the unperturbed background IGM prior to reionization (see Section 2), as was required to enable baryons to collapse into the halo along with dark matter. Their 'Strömgren numbers' $L_S \equiv 2R_{\rm halo}/\ell_S$, the ratio of the diameter of a halo to the Strömgren length ℓ_S inside the halo (the length of a column of gas within which the unshielded arrival rate of ionizing photons just balances the total recombination rate), were large. For a uniform gas of H density n_H, located a distance $r_{\rm Mpc}$ (in Mpc) from an ultraviolet (UV) source emitting $N_{\rm ph,56}$ ionizing photons (in units of 10^{56} s^{-1}), the Strömgren length is only $\ell_S \approx (100\,{\rm pc})\,(N_{\rm ph,56}/r_{\rm Mpc}^2)\,(n_H/0.1\ {\rm cm}^{-3})^{-2}$, so $L_S \gg 1$ for most of the range of halo masses and sources of interest, as we will discuss in Section 2.3. In that case, the intergalactic, weak, R-type I-front which entered each minihalo during reionization would have decelerated to about twice the sound speed of the ionized gas before it could exit the other side, thereby transforming itself into a D-type front, preceded by a shock. Typically, the side facing the source would then have expelled a supersonic wind backwards toward the source, which shocked the surrounding IGM as the minihalo photoevaporated.

The importance of this photoevaporation process has long been recognized in the study of interstellar clouds exposed to ionizing starlight (Oort & Spitzer 1955; Spitzer 1978; Bertoldi 1989; Bertoldi & McKee 1990; Lefloch & Lazareff 1994; Bertoldi & Draine 1996; Lizano et al. 1996; Gorti & Hollenbach 2002). Radiation-hydrodynamical simulations were performed in 2D of a stellar I-front overtaking a clump inside a molecular cloud (Klein, Sandford & Whitaker 1983; Sandford, Whitaker & Klein 1983). More recently, 2D simulations for the case of a circumstellar cloud ionized by a single nearby star have also been performed (Mellema et al. 1998). In the cosmological context, however, the importance of this process has only recently been fully appreciated.

In proposing the expanding minihalo model to explain Lyman α forest (LF) quasar absorption lines, Bond, Szalay & Silk (1988) discussed how gas originally confined by the gravity of dark minihaloes in the cold dark matter (CDM) model with virial temperatures below 10^4 K would have been expelled by pressure forces if photoionization by ionizing background radiation suddenly heated all the gas to an isothermal condition at $T \approx 10^4$ K, a correct description only in the optically thin limit. The first realistic discussion of the photoevaporation of such minihaloes by cosmological I-fronts, including the first radiation-hydrodynamical simulations of this process, was by Shapiro, Raga & Mellema (1997, 1998). This work demonstrated the importance of taking proper account of optical depth and self-shielding simultaneously with hydrodynamics, in order to derive the correct dynamical flow, ionization structure and the resulting observational characteristics. Barkana & Loeb (1999) subsequently confirmed the relative importance of this process as a feedback effect on dwarf-galaxy minihaloes during reionization, using static models of uniformly illuminated spherical clouds in thermal and ionization equilibrium, without accounting for gas dynamics. They took H-atom self-shielding into account and assumed that all gas which is instantaneously heated above the minihalo virial temperature must be evaporated. They concluded that 50–90 per cent of the gas in gravitationally bound objects when reionization occurred should have been evaporated. However, by neglecting the time-dependent gas dynamical nature of this phenomenon, their model failed to capture some essential physics, leading to incorrect results, as we will show below.

Further results of radiation-hydrodynamical simulations of a cosmological minihalo overrun by a weak, R-type I-front in the surrounding IGM were summarized in Shapiro & Raga (2000a,b, 2001) and Shapiro (2001). These results were preliminary versions of the final, more advanced results which we shall present in this paper in some detail. Before we do, it is worth summarizing why we believe that the particular problem simulated here is not only generic to the minihaloes which formed prior to the end of the reionization epoch, but likely to have affected the global outcome of cosmic reionization, as well.

According to the currently prevalent paradigm of cosmic structure formation – the flat, cold dark matter universe with cosmological constant (ΛCDM) – cosmological structures formed hierarchically, with small-mass haloes forming first and merging over time to form ever larger haloes. The first baryonic structures to emerge in this way were the 'minihaloes' which began forming at $z > 20$–30, with masses in the range from about 10^4 M$_\odot$ to 10^8 M$_\odot$, where the minimum is set by the Jeans mass in the cold and neutral IGM prior to its reionization. The term 'minihalo' used here specifically refers to haloes at any epoch with virial temperatures $T_{\rm vir} \leqslant 10^4$ K. In such haloes, the thermal collisional ionization rate alone was not sufficient to ionize the H and He atoms significantly, so the minihalo gas was almost entirely neutral, in the absence of ionizing radiation. Moreover, collisional line excitation of H atoms is exponentially suppressed below 10^4 K and, thus, a purely atomic gas of H and He could not radiatively cool effectively below that temperature. Such minihalo gas was able to cool below 10^4 K only if H_2 molecules formed in sufficient abundance to cool it by rotational–vibrational line excitation, to temperatures as low as $T \lesssim 100$ K. This H_2 formation, catalysed by the tiny residual ionized fraction, was essential if the minihalo gas was to cool and, thereby, compress relative to the dark matter, enough to become self-gravitating and form stars. Simulations suggest that minihaloes of mass $M \gtrsim 10^6$ M$_\odot$ did just that, thereby forming the first metal-free ('Population III') stars of mass $M_* \gtrsim 100$ M$_\odot$ at $z \lesssim 30$ (Abel, Bryan & Norman 2002; Bromm, Coppi & Larson 2002), perhaps leading to the first miniquasars, as well.

While this process of star formation in minihaloes is important as the origin of the first sources of ionizing radiation in the Universe, minihaloes are not likely to have been the dominant source of cosmic reionization. The H_2 formation required for minihaloes to form stars would have been suppressed easily by photodissociation in the Lyman–Werner bands by the background of UV radiation created by the very first minihaloes which formed stars, when the ionizing radiation background was still much too low to cause reionization (Haiman, Abel & Rees 2000). If so, most minihaloes must not have formed stars and must, instead, have remained 'sterile', dark-matter-dominated haloes filled with stable, neutral atomic gas at the halo virial temperature $T_{\rm vir} \leqslant 10^4$ K. In that case, when some

other source of radiation ionized the Universe and drove an I-front into the minihalo, which photoheated the gas to $T > 10^4$ K, minihalo gravity would have been unable to confine the ionized gas and, eventually, all of it was expelled. A caveat to this description above of the negative feedback on the H_2 in minihaloes due to the first UV sources is the possibility that the presence of a weak X-ray background might have counterbalanced this H_2 photodissociation by enhancing the H_2 formation rate in places where X-ray ionization increased the small ionized fraction inside the haloes (Haiman et al. 2000).[2] Other recent papers (Machacek, Bryan & Abel 2001, 2003; Ricotti, Gnedin & Shull 2001, 2002b; Yoshida et al. 2003) suggest that both the negative feedback due to UV radiation and the possible positive feedback due to an X-ray background may have been overestimated by Haiman et al. (2000). Apart from such caveats, however, the primary source of reionizing photons is believed to have been the haloes with $T_{\rm vir} \geqslant 10^4$ K. For such haloes, radiative cooling by H-atom line excitation alone was efficient enough to compress the gas to enable self-gravity and self-shielding, leading to star formation. For the purposes of this paper, we shall henceforth accept the premise that the minihaloes were predominantly 'sterile' targets of source haloes with $T_{\rm vir} \geqslant 10^4$ K, of higher mass.

In that case, it has been shown that source haloes would generally have found their skies covered by the minihaloes between them and neighbouring source haloes, until the ionization fronts created by those sources overtook the minihaloes and photoevaporated them, possibly consuming a significant fraction of the ionizing photons released by the sources in the process (Haiman, Abel & Madau 2001; Shapiro 2001; Barkana & Loeb 2002; Shapiro et al. 2003). According to these authors, the phenomenon of minihalo photoevaporation during reionization identified by Shapiro et al. (1997, 1998) not only was quite common and had an important negative feedback effect on the minihaloes, it also had an important effect on reionization itself, by screening the ionizing sources and increasing the number of ionizing photons required per baryon to complete reionization. While these results demonstrate the importance of minihaloes to the cosmic reionization story, we will show that a correct quantitative estimate of these effects requires detailed gas dynamics and radiative transfer simulations. In addition, as pointed out by Shapiro (2001), there is a very large number of minihaloes per unit redshift along an arbitrary line of sight (LOS) through the Universe at $z \geqslant 6$, so the process of their photoevaporation is potentially observable in the absorption spectra of very high-z sources, like quasi-stellar objects (QSOs), supernovae, bright starburst galaxies, and gamma-ray burst (GRB) afterglows.

This paper is organized as follows. In Section 2, we discuss our minihalo model and the statistics of minihaloes in the ΛCDM universe, as well as the analytical expectations for how the photoevaporation of cosmological minihaloes proceeds and what its outcome is. In Section 3, we outline the basic equations used to model the gas dynamics of photoevaporation, the microphysical processes considered and the initial conditions for our simulations. In Section 4, we discuss our numerical method and tests, and the parameters of our simulations. In Section 5, we describe the photoevaporation process in detail for the illustrative case of a minihalo of 10^7 $M_\odot$ at $z = 9$ exposed to ionizing radiation from one of three types of sources: (1) starlight with a 50 000 K black-body spectrum (hereafter, referred to as 'BB 5e4'), representative of massive Population II stars, (2) starlight with a 10^5 K black-body spectrum (hereafter, 'BB 1e5'), as expected for massive Population III stars, and (3) QSO-like, with a power-law spectrum $F_\nu \propto \nu^{-1.8}$ ($\nu > \nu_{\rm H}$) (hereafter, 'QSO'). We show our results for the structure of the global I-front propagating in the IGM during its weak, R-type phase (Section 5.1), the encounter between this global I-front and a minihalo along its path and the penetration of the minihalo by the front in its weak, R-type phase (Section 5.2), the trapping of the I-front inside the minihalo and its transition to D-type (Section 5.3), the structure of the photoevaporative flow during the D-type phase (Section 5.4), the evolution of temperature structure (Section 5.5) and I-front location and speed (Section 5.6), the evaporation times (Section 5.7), the consumption of ionizing photons (Section 5.8), and some observational diagnostics (Section 5.9). Finally, in Section 6, we give our summary and conclusions.

[2] The net effect of these early X-rays on the H_2 in minihaloes may have been more negative than positive, however, if they raised the entropy floor of the IGM from which the minihaloes condensed (Oh & Haiman 2003).

2 ANALYTICAL CONSIDERATIONS

2.1 Cosmological minihaloes during reionization in a ΛCDM universe

2.1.1 Minihalo model

Our initial minihalo model consists of a virialized region in hydrostatic equilibrium embedded in an exterior region of cosmological infall. For the former, we have previously developed an analytical model for the post-collapse equilibrium structure of virialized objects that condense out of a cosmological background universe, either matter-dominated or flat with a cosmological constant (Shapiro, Iliev & Raga 1999; Iliev & Shapiro 2001). This truncated isothermal sphere, or TIS, model assumes that cosmological haloes form from the collapse and virialization of 'top-hat' density perturbations and are spherical, isotropic and isothermal. This leads to a unique, non-singular TIS, a particular solution of the Lane–Emden equation (suitably modified when $\Lambda \neq 0$). The size r_t and velocity dispersion σ_V are unique functions of the mass M and formation redshift $z_{\rm coll}$ of the object for a given background universe. The TIS profile flattens to a constant central value, ρ_0, which is roughly proportional to the critical density of the Universe at the epoch of collapse, $\rho_c(z_{\rm coll})$, with a small core radius $r_0 \approx r_t/30$ [where $\sigma_V^2 = 4\pi G\rho_0 r_0^2$ and $r_0 \equiv r_{\rm King}/3$ for the 'King radius' $r_{\rm King}$, defined by Binney & Tremaine (1987), p. 228]. While the TIS model does not produce the central cusp at very small radii in the dark matter density profile of haloes predicted by numerical CDM N-body simulations, it does reproduce many of the average properties of these haloes remarkably well, suggesting that it is a useful approximation for haloes which result from more realistic initial conditions (Shapiro et al. 1999; Iliev & Shapiro 2001, 2003). In particular, the TIS mass profile agrees well with the fit by Navarro, Frenk & White (1996, 1997, hereafter NFW) to numerical simulations (i.e. fractional deviation $\lesssim$20 per cent) at all radii outside of a few TIS core radii (i.e. outside a King radius or so). Our application here of the TIS model is not sensitive to the small difference between the TIS and NFW dark-matter density profiles at small radii. In both cases, the baryonic profile is non-singular.

The TIS halo is uniquely specified by the central density ρ_0 and core radius r_0. Since the central density is proportional to $\rho_c(z_{\rm coll})$, it is also possible to specify the profile by the two parameters, total mass and collapse redshift (M, $z_{\rm coll}$), which is equivalent to specifying the pair (r_0, ρ_0). This makes the TIS model extremely useful in combination with other analytical methods which determine the typical epochs of collapse for haloes of different masses, such as

the well-known Press–Schechter approximation. We note that it is customary elsewhere to define the total mass of profiles used to model CDM haloes as M_{200}, the mass inside a sphere of radius r_{200} with a mean density which is 200 $\rho_c(z)$ at some redshift z. For the sake of comparison with the TIS profile, if we were to fix M_{200} and r_{200} for haloes of different profiles, which amounts to fixing M and $z_{\rm coll}$ for the TIS halo, then $M = 1.167 M_{200} = 772.6\rho_0 r_0^3$, $\rho_0 = 18\,000\rho_c(z_{\rm coll})$ and $r_{200} = 24.2 r_0$ if $z = z_{\rm coll}$.

As applied here to model minihaloes, the TIS is embedded in a self-similar, spherical, cosmological infall, using the solution for the latter in an Einstein–de Sitter universe derived by Bertschinger (1985), generalized by us to apply it to a low-density background universe at the early times considered here (Iliev & Shapiro 2001, Appendix A). As discussed in detail in Shapiro et al. (1999) and Iliev & Shapiro (2001), the truncation radius of the TIS solution coincides almost exactly with the location of the shock in the self-similar infall solution, allowing a natural match of the two models. The procedure which we used to accomplish that is discussed in detail in Appendix A.

For the calculations in this paper, our fiducial case is a minihalo of mass $M = 10^7$ M$_\odot$ which collapses at $z = 9$. According to the TIS model, this minihalo has a virial radius $r_t = 0.76$ kpc, a virial temperature $T_{\rm vir} = 4000$ K, and a dark matter (DM) velocity dispersion $\sigma_V = 5.2$ km s^{-1}. In units of these fiducial values, we define $M_7 \equiv M/(10^7$ M$_\odot$) and $(1+z)_{10} \equiv (1+z)/10$. We shall express temperature in terms of $T_4 = T/(10^4$ K).

2.1.2 *Statistical properties of minihaloes*

This TIS model for the internal structure of an individual minihalo of a given mass M which forms at a given collapse epoch $z_{\rm coll}$ can be combined with the Press–Schechter (PS) approximation to determine the statistical expectations for the properties of haloes of different masses at each epoch which result from the Gaussian-random initial fluctuations of the ΛCDM universe.

In Fig. 1, we plot the curves in the M–$z_{\rm coll}$ plane of the halo which correspond to haloes which collapse from ν–σ fluctuations for $\nu = 1$, 2, and 3. Here $\nu \equiv \delta_{\rm crit}/\sigma(M)$, $\sigma(M)$ is the rms fluctuation in the dark matter density field, filtered on mass scale M, as predicted by linear theory, and $\delta_{\rm crit}$ is the overdensity of a top-hat perturbation given by extrapolating the linear solution to the time of infinite collapse in the exact non-linear solution. The value $\nu = 1$ corresponds to the most common haloes, while high values of ν correspond to rare density peaks.

The minihaloes span a mass range from $M_{\rm min}$ to $M_{\rm max}$ which varies with redshift, with $M_{\rm min}$ close to the Jeans mass of the uncollapsed IGM prior to reionization,

$$M_{\rm J} = 5.7 \times 10^3 {\rm M}_\odot \left(\frac{\Omega_0 h^2}{0.15}\right)^{-1/2} \left(\frac{\Omega_{\rm b} h^2}{0.02}\right)^{-3/5} (1+z)_{10}^{3/2}, \quad (1)$$

while

$$M_{\rm max} = 3.95 \times 10^7 {\rm M}_\odot \left(\frac{\Omega_0 h^2}{0.15}\right)^{-1/2} (1+z)_{10}^{-3/2} \quad (2)$$

is the mass for which $T_{\rm vir} = 10^4$ K according to the TIS model (Iliev & Shapiro 2001). This maximum minihalo mass at each epoch (i.e. the curve of constant $T_{\rm vir} = 10^4$ K) is shown in Fig. 1, which demonstrates that, below redshift $z \sim 10$, all minihaloes result from fluctuations with $\nu < 2$, so they are quite typical and fairly common. Integrating over the entire mass function of minihaloes from $M_{\rm min}$ to $M_{\rm max}$, we find that the total collapsed mass fraction in minihaloes is 36, 28, 10 and 3 per cent at $z = 6$, 9, 15, 20, respectively.

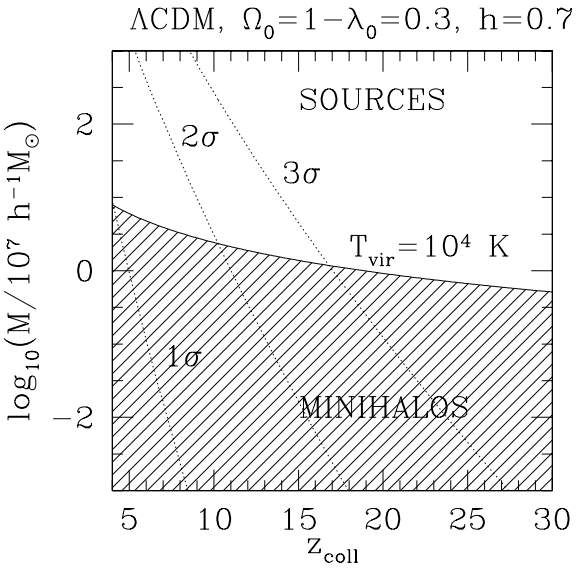

Figure 1. How common are minihaloes at high redshift? Plot of minihalo mass versus redshift. The shaded region represents minihaloes: haloes with virial temperature $T_{\rm vir} < 10^4$ K. Dotted curves represent ν–σ fluctuations with $\nu = 1$, 2 and 3, predicted by the PS approximation, as labelled.

Our description above of the mass function of minihaloes which contain neutral gas assumes that the IGM out of which the minihalo baryonic component collapsed was not yet reheated by the energy release associated with the first sources. The reheating of the IGM which results when the first sources turn on and reionization begins can inhibit the further collapse of baryons into newly formed minihaloes, thereafter (e.g. Shapiro, Giroux & Babul 1994; Gnedin 2000b; Haiman, Abel & Madau 2001; Venkatesan, Giroux & Shull 2001; Oh & Haiman 2003). In that case, one must filter the mass function of CDM minihaloes below a mass scale which is greater than $M_{\rm min}$ in equation (1) when applying it to describe haloes which contain not only dark matter, but baryons as well. In regions of the IGM which have not yet been reionized, however, the *unfiltered* halo mass function for $M \geqslant M_{\rm min}$ based on equation (1) still applies to the minihaloes with neutral gas, *even after reionization is underway*. As described in Section 1.1, current observations indicate that reionization began at $z \gtrsim 15$ but was not complete until $z \sim 6$, so it is reasonable to suppose that reionization proceeded in a patchy way over this extended period of time, with some patches surviving in a neutral state until the end of reionization at $z \sim 6$.

2.2 Ionizing flux

We shall assume that each minihalo is photoevaporated by an isotropic point source located at a proper distance r from the minihalo centre, which emits $N_{\rm ph}$ H ionizing photons per second with luminosity L_ν (erg s^{-1}Hz^{-1}), so that

$$N_{\rm ph} = \int_{\nu_{\rm H}}^{\infty} {\rm d}\nu \frac{L_\nu}{h\nu}. \quad (3)$$

The unattenuated flux at the location of the minihalo centre is just $F_\nu = L_\nu/(4\pi r^2)$, since $r \ll c/H(z)$, the horizon size during minihalo photoevaporation. We shall, henceforth, parameterize the flux to which a given halo is exposed in terms of the dimensionless

frequency-integrated photon flux, $F_0 \equiv N_{\rm ph,56}/r^2_{\rm Mpc}$. For example, a source which emits 10^{56} (or 10^{52}) ionizing photons per second at a distance of 1 Mpc (or 10 kpc) corresponds to $F_0 = 1$, or, in physical units, a flux of 8.356×10^5 cm^{-2} s^{-1}. What values of F_0 are relevant to the encounter between a minihalo and an I-front during cosmic reionization?

To get a sense of how large this fiducial flux is in terms of an equivalent isotropic radiation background, we can estimate the mean ionizing photon intensity J_γ (cm^{-2} s^{-1} ster^{-1}) required to irradiate an atom on the minihalo surface with the same flux, by equating this flux to $2\pi J_\gamma$. For a QSO-like ionizing background with a power-law energy spectrum, $J_\nu \propto \nu^{-\alpha}$, $\alpha > 1$, for example, the integrated photon intensity is $J_\gamma = 1.509 \times 10^5 J_{-21}(1+\alpha)^{-1}$, where J_{-21} is the mean intensity at the H Lyman limit in units of 10^{-21} erg cm^{-2} s^{-1} Hz^{-1} ster^{-1}. The equivalent dimensionless flux parameter is then given by

$$F_{0,\rm equ} = 1.13(1+\alpha)^{-1} J_{-21}, \tag{4}$$

so $F_0 = 1$ is roughly equivalent to $J_{-21} \sim 1$.

We can estimate the appropriate range to consider for F_0 as follows. Suppose the luminosity of a dwarf galaxy is produced by a super-massive star cluster (SSC). Tan & McKee (2001) estimate the ionizing luminosity of such an SSC, using the observed stellar mass function in the R136 cluster in 30 Doradus as input to the STARBURST99 code of Leitherer et al. (1999), finding (for $0.1 \leqslant M_*/{\rm M}_\odot \leqslant 100$)

$$N_{\rm ph,52} = 3.94 M_{*,6}, \tag{5}$$

where M_* is the total mass in stars, $M_p \equiv M/(10^p\ {\rm M}_\odot)$ and $N_{\rm ph,q} \equiv N_{\rm ph}/(10^q\ {\rm s}^{-1})$ is the flux of ionizing photons.

Alternatively, Madau & Rees (2000) have estimated that, for a standard Salpeter initial mass function (IMF), approximately 3000–4000 ionizing photons are emitted for every stellar baryon. Hence, if the galaxy gas mass turned into stars is M_*, the total number of ionizing photons emitted during the lifetime of those stars is

$$N_{\rm tot} = \int N_{\rm ph} {\rm d}t \approx 10^{66.6} M_{*,6}. \tag{6}$$

Assuming an average lifetime of $\tau_{\rm lifetime} \approx 10^7$ yr, we obtain

$$N_{\rm ph,52} \approx 1.6 M_{*,6}, \tag{7}$$

similar to the result in equation (5). On the other hand, Bromm, Kudritzki & Loeb (2001) estimate that the number of photons produced per baryon by Population III stars can be about 10–20 times higher than this.

If we let $f_{\rm b} = \Omega_{\rm b}/\Omega_0 = 0.136$ be the cosmic mean baryonic mass fraction and f_* be the fraction of these baryons which are converted into stars in the dwarf galaxy halo, then $M_* = f_* f_{\rm b} M_{\rm halo}$. Tan & McKee (2001) find $f_* = 0.5$ for their SSC. If the target minihalo mass $M_{\rm target} \ll M_{\rm halo}$, the mean distance between source and halo is $r \approx d_{\rm sep}/2$, while if $M_{\rm target} \approx M_{\rm halo}$, it is $r = d_{\rm sep}$. For source haloes of mass 10^8 M$_\odot$ at $z = 9$, $d_{\rm sep} \approx 50$ kpc (Shapiro 2001), so $r_{\rm Mpc} = (0.5-1) \times d_{\rm sep,Mpc} \approx 0.025$–$0.05$. The characteristic dimensionless flux F_0 for such sources at this epoch is, therefore, given by

$$F_0 = \frac{N_{\rm ph,56}}{r^2_{\rm Mpc}} = (1-4) \times 3.94 \times 10^{-2} \frac{f_* f_{\rm b} M_{\rm halo,8}}{d^2_{\rm sep,Mpc}} \approx 1-4, \tag{8}$$

if we adopt the luminosity per gas mass estimated by Tan & McKee (2001). For haloes in the dwarf-galaxy mass range, the Press–Schechter (PS) approximation for the halo mass function in ΛCDM yields ${\rm d}n_{\rm halo}/{\rm d}M \propto M^{-2}$ (Shapiro 2001), so the mean separation of dwarf-galaxy sources of mass M is $d_{\rm sep} = (M\ {\rm d}n_{\rm halo}/{\rm d}M)^{-1/3} \propto M^{1/3}$. If the mass-to-light ratio M/L is independent of halo mass, then the flux incident on a minihalo due to one of these haloes scales only weakly with source halo mass, $F_0 \propto M^{1/3}$, up to the galaxy mass scale above which the PS mass function cuts off exponentially, at which point F_0 drops rapidly with increasing mass.

Finally, we can get a simple, direct estimate of F_0 based on the mean flux required to reionize the Universe, as follows. Suppose the Universe was filled with sources that supplied $\bar{\xi}$ ionizing photons per H atom steadily over the time between the source turn-on epoch $z_{\rm on}$ and the epoch of reionization overlap at $z_{\rm ov}$. Assuming that all photons remained energetic enough to ionize H atoms despite their continuous redshifting, and neglecting the absorption of these photons during the extended reionization epoch, the mean comoving number density of ionizing photons at any redshift in the range $z_{\rm on} \leqslant z \leqslant z_{\rm ov}$ would be just

$$\bar{n}_\gamma = \bar{\xi} \bar{n}_{\rm H} \frac{t(z) - t_{\rm on}}{t_{\rm ov} - t_{\rm on}}, \tag{9}$$

where t is the age of the Universe at each redshift, as labelled, and $\bar{n}_{\rm H}$ here refers to the mean IGM H density. The mean photon intensity J_γ of this isotropic background of ionizing radiation would then be given by

$$J_\gamma = \frac{c}{4\pi} \bar{n}_\gamma = \frac{\bar{\xi} \bar{n}_{\rm H} c}{4\pi} \frac{t(z) - t_{\rm on}}{t_{\rm ov} - t_{\rm on}}. \tag{10}$$

This corresponds to an effective photon flux $F_{\rm eff}$ given by

$$F_{\rm eff} = 2\pi J_\gamma = \frac{\bar{\xi} \bar{n}_{\rm H} c}{2} \frac{t(z) - t_{\rm on}}{t_{\rm ov} - t_{\rm on}}, \tag{11}$$

or a dimensionless flux

$$F_{0,\rm eff} = 3\bar{\xi}\ (1+z)^3_{10} \left(\frac{\Omega_{\rm b} h^2}{0.02}\right) \left[\frac{t(z) - t_{\rm on}}{t_{\rm ov} - t_{\rm on}}\right]. \tag{12}$$

For $t_{\rm on} \ll t_{\rm ov}$ the quantity in square brackets can be replaced by $t(z)/t_{\rm ov}$ to yield an upper limit,

$$F_{0,\rm eff} \lesssim 3\bar{\xi} (1+z)^3_{10} \left(\frac{\Omega_{\rm b} h^2}{0.02}\right) \left(\frac{1+z}{1+z_{\rm ov}}\right)^{-3/2}, \tag{13}$$

or, if $z_{\rm ov} = 6$ and $\Omega_{\rm b} h^2 = 0.02$,

$$F_{0,\rm eff} \lesssim 1.8\bar{\xi}\ (1+z)^{3/2}_{10}. \tag{14}$$

This suggests that $F_0 \sim 1$ is a reasonable fiducial choice for the flux to which minihaloes were exposed during reionization before overlap. In this paper we present results for $F_0 = 1$ only. We defer the study of the effects of varying F_0 to the companion paper, where we shall present results for F_0 in the range from 0.01 to 10^3.

2.3 Minihalo Strömgren numbers and I-front trapping

2.3.1 I-front trapping

For a spherical H II region in a uniform interstellar gas, the early expansion phase of the weak, R-type I-front ends when the I-front decelerates to twice the sound speed of the ionized gas, at which point it makes the transition from R-critical to D-critical, preceded by a shock front (Spitzer 1978). This transition occurs when the radius of the I-front approaches that of the Strömgren sphere. By analogy, we expect our intergalactic, weak, R-type I-front to make a similar transition to D-type after it enters a minihalo when it slows to the R-critical speed as it travels up the density gradient inside the minihalo, a distance comparable to the Strömgren length along its path through the halo. In order to 'trap' the I-front, therefore, the

minihalo size must exceed this length. We can estimate the 'trapping' condition as follows.

The Strömgren length $\ell_S(r)$ at impact parameter r is given by

$$F = \int_0^{\ell_S(r)} \mathrm{d}\ell n_e n_H \alpha_H^{(2)}, \quad (15)$$

i.e. by balancing the number of recombinations with the number of ionizing photons arriving along a given LOS.[3] The integration in equation (15) is done along the LOS, n_H is the H number density, n_e is the electron density, F is the flux of ionizing photons, $\alpha_H^{(2)}$ is the case B recombination coefficient for hydrogen, and we have assumed for simplicity that only the H in the gas is ionized. We then define the 'Strömgren number' for the halo as $L_S \equiv 2r_t/\ell_S(0)$, where r_t is the radius of the halo and $\ell_S(0)$ is the Strömgren length for zero impact parameter. If $L_S > 1$, then the halo is able to trap the I-front, while if $L_S < 1$, the halo would be ionized quickly by the passage of the weak, R-type I-front across it, which will not slow down enough to be trapped. In the latter case, if $L_S \ll 1$, the halo gas would be uniformly photoheated to $T \geqslant 10^4$ K before any mass motions could occur, and the pressure gradient would blow the gas apart isotropically, long after the I-front had exited the halo.

The threshold condition $L_S = 1$ is equivalent to

$$F = \frac{2\alpha_H^{(2)} f_b^2}{(\mu_H m_H)^2} \rho_0^2 r_0 \int_0^{\zeta_t} \tilde{\rho}^2(\zeta)\, \mathrm{d}\zeta, \quad (16)$$

where $\tilde{\rho} \equiv \rho/\rho_0$, $\zeta \equiv r/r_0$, $f_b = \Omega_b/\Omega_0$ is the baryonic mass fraction and $\mu_H m_H$ is the mean gas mass per H atom. The dependences on the source flux and on the minihalo mass and size at different redshift are combined if we define the parameter

$$\chi_S \equiv \frac{F}{\rho_0^2 r_0} = \chi_{S,0} F_0 M_7^{-1/3} (1+z)_{10}^{-5} \left(\frac{\Omega_0 h^2}{0.15}\right)^{-5/3}, \quad (17)$$

where $M_7 \equiv M_{tot}/(10^7\ \mathrm{M}_\odot)$ and $\chi_{S,0} \equiv 4.1 \times 10^{30}\ \mathrm{g^{-2}\ cm^3\ s^{-1}}$. We have used the fact that $I \equiv 2\int_0^{\zeta_t} \tilde{\rho}^2(\zeta)\mathrm{d}\zeta = 3.49$ and the scalings of ρ_0 and r_0 with the mass of the halo and its redshift of collapse according to the TIS model at high redshift (Iliev & Shapiro 2001). There is a direct correspondence between L_S and χ_S, and the condition $L_S = 1$ is equivalent to $\chi_S = \chi_{S,crit}$ where

$$\chi_{S,crit} = 3.3 \times 10^{33} T_4^{-3/4} \left(\frac{\Omega_b h^2}{0.02}\right)^2 \left(\frac{\Omega_0 h^2}{0.15}\right)^{-2} \mathrm{g^{-2}\ cm^3\ s^{-1}} \quad (18)$$

(where T_4 refers to the temperature of the ionized gas) while $L_S > 1$ and $L_S < 1$ correspond to $\chi_S < \chi_{S,crit}$ and $\chi_S > \chi_{S,crit}$, respectively. We plot $\ell_S(0)$ versus χ_S in Fig. 2. For our fiducial case, $\chi_S = \chi_{S,0} \ll \chi_{S,crit}$, so we expect the I-front to be easily trapped by the minihalo in this case. In general, the critical minihalo mass which is just large enough to trap the I-front by making $L_S = 1$ is given by setting $\chi_S = \chi_{S,crit}$ in equation (17) to yield

$$M_{7,crit} = 1.8 \times 10^{-9} F_0^3 [(1+z)_{10}]^{-15} T_4^{9/4} \left(\frac{\Omega_0 h^2}{0.15}\right) \left(\frac{\Omega_b h^2}{0.02}\right)^{-6}. \quad (19)$$

For $F_0 \lesssim 10$, even the smallest minihaloes which formed at the last possible moment before the I-front overtook them at the end of the reionization epoch at $z_{ov} = 6$ would have been able to trap the I-front.

[3] We have adapted cylindrical coordinates (r, x) in which the x-axis is the line between the source and the minihalo centre, the axis of symmetry of this problem. In writing equation (15), we have assumed that the distance between the source and the minihalo is much greater than the size of the minihalo, so we can approximate the LOS as parallel to the x-axis.

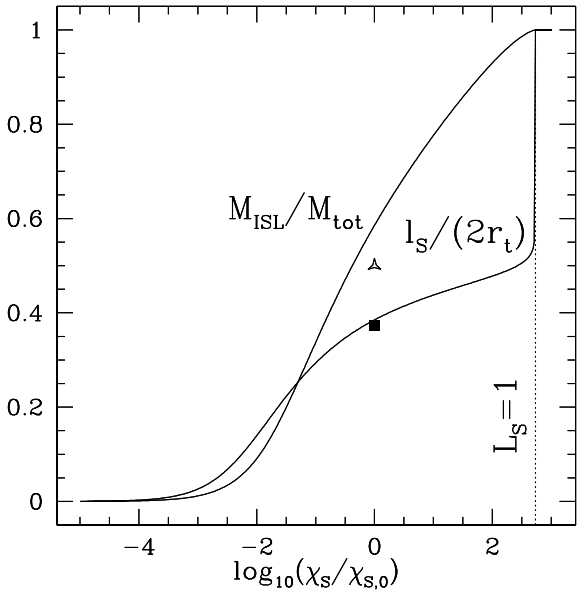

Figure 2. Inverse Strömgren layer (ISL). The Strömgren length along the axis, $l_S(0)$, in units of the halo diameter $2r_t$ and ISL mass M_{ISL} in units of the total mass M_{tot} versus $\chi_S/\chi_{S,0}$, where $\chi_S \equiv F/(\rho_0^2 r_0)$, $\chi_{S,0}$ is χ_S for our fiducial halo and $F_0 = 1$. Symbols indicate the (roughly) corresponding simulation results for M_{ISL}/M_{tot} (star) and $\ell_S(0)/(2r_t)$ (square) at the moment of I-front transition from R-type to D-type (see Section 5.2). The dotted line indicates the value $\chi_{S,crit}$ for which $L_S = 1$. We assume $T_4 = 2$.

For a uniform halo with gas number density $\langle n_H \rangle$, equation (15) reduces to

$$\ell_S = \frac{F}{\alpha_H^{(2)} \langle n_H \rangle^2}. \quad (20)$$

In terms of the I-front trapping condition ($L_S = 1$), a TIS halo with mean density $\bar{\rho}_{TIS}$ is equivalent to a uniform halo of the same size but with mean density given by

$$\bar{\rho} = \rho_0 \left(\frac{I}{2\zeta_t}\right)^{1/2} = 0.24\rho_0 = 34\bar{\rho}_{TIS}, \quad (21)$$

where $\bar{\rho}_{TIS}$ is the mean density of the TIS. Hence, a uniform halo of the same size as the TIS minihalo which is just large enough to trap the I-front will do so only if it is 34 times more massive than the TIS halo.

One important implication of this result is that it would be incorrect to use the volume-average mean density of a minihalo instead of this much larger density in equation (21) to determine whether a minihalo of a given mass will trap the I-front. In particular, if we replace the realistic TIS profile of the centrally concentrated minihalo by a uniform-density minihalo with the same mass and radius, instead, the Strömgren number, $L_{S,uniform}$, of this uniform halo will be very much smaller than L_S for the TIS minihalo, according to

$$L_{S,uniform} = 8.9 \times 10^{-4} (\chi_{S,crit}/\chi_S) = 0.72 M_7^{1/3} (1+z)_{10}^5 F_0^{-1} T_4^{-3/4} \left(\frac{\Omega_b h^2}{0.02}\right)^2 \left(\frac{\Omega_0 h^2}{0.15}\right)^{-1/3}. \quad (22)$$

Hence, when a TIS minihalo of a given mass is just marginally able to trap the I-front (i.e. $\chi_S = \chi_{S,crit}$), a uniform halo with the same mass and radius has a Strömgren number $L_S = 8.9 \times 10^{-4}$, far below the minimum required to trap the I-front! This means that the phenomenon of I-front trapping can be missed entirely by numerical

simulations of reionization which do not fully resolve the internal structure of individual minihaloes, even when their resolution in mass and length are, in principle, high enough to identify minihaloes of the correct mass and mean density. For this reason, the simulations we shall report here are high enough in resolution to guarantee that the internal structure of individual minihaloes is fully resolved.

2.3.2 Inverse Strömgren layer in a minihalo

We define the inverse Strömgren layer (ISL) as the region inside the minihalo which is the H II region predicted by the Strömgren approximation. This region is bounded by the minihalo surface nearest to the source and by the surface defined at each impact parameter r by $\ell_S(r)$ in equation (15). This ISL provides an estimate of the minihalo region which will be ionized first, during the weak, R-type I-front phase, and of the approximate location of the surface inside the minihalo where the transition to D-type will occur as the R-type front approaches it. In Fig. 2, we show the fraction of the halo mass which is located inside the ISL, $M_{\rm ISL}/M_{\rm tot}$, versus χ_S, given by

$$M_{\rm ISL} = \int_0^{r_t} 2\pi r\, {\rm d}r \int_0^{\ell_S(r)} \rho(R)\, {\rm d}X. \tag{23}$$

Here $R = \{r^2 + [X - (r_t^2 - r^2)^{1/2}]^2\}^{1/2}$. In Fig. 2 we also plot $L_S^{-1} = \ell_S(0)/(2r_t)$ (the Strömgren length for $r = 0$ in units of the halo diameter) versus χ_S, and we indicate the corresponding simulation results at the approximate moment of transition of the I-front from R-type to D-type, to be discussed in Section 5.2. At $\chi_S = \chi_{S,\rm crit}$, the ISL includes the entire minihalo, thus $M_{\rm ISL}/M_{\rm tot} = 1$ and $\ell_S(0) = 2r_t$. In Fig. 3, we plot the shape of the ISL surface for $\chi_S/\chi_{S,0} =$ 0.01, 0.1, 1, 10, 100, and 250. We see that, even for low values of the parameter χ_S (equivalent to low external flux levels) a significant fraction of the halo volume becomes ionized quickly due to the relatively low density in the halo outskirts. However, from Fig. 2 we see that this volume still corresponds to a small fraction of the total mass (e.g. for $\chi_S/\chi_{S,0} < 0.01$, $M_{\rm ISL} < 10$ per cent). As χ_S approaches $\chi_{S,\rm crit}$, the neutral gas fraction shielded by the highly concentrated halo core diminishes until it disappears completely when $\chi_S = \chi_{S,\rm crit} = 490\chi_{S,0}$ (for $T_4 = 2$).

2.4 Evaporation time

A rough, order-of-magnitude guide to the time-scale $t_{\rm ev}$ for minihalo photoevaporation is the sound-crossing time for the characteristic size of the minihalo at the sound speed of the ionized gas, $t_{\rm sc} = 2r_t/c_s(10^4\ {\rm K})$. The actual I-front propagation and evaporative wind are quite complex, as we shall see, and depend upon additional properties like the halo mass and density, flux level and spectrum, and the time it takes the halo and background Universe to evolve. However, this simple estimate will be a convenient standard of reference with which to compare the actual simulation results.

For a minihalo of mass M at high redshift, we obtain

$$t_{\rm sc} = 98\ {\rm Myr}\,(M_7)^{1/3}\left(\frac{\Omega_0 h^2}{0.15}\right)^{-1/3}(1+z)_{10}^{-1}, \tag{24}$$

using the adiabatic sound speed $c_s(10^4\ {\rm K}) = 11.7(T_4/\mu)^{1/2} = 15.2\ T_4^{1/2}\ {\rm km\ s^{-1}}$, where $\mu = 0.59$ is the mean molecular weight for fully ionized gas of H and He if the abundance of He is $A({\rm He}) = 0.08$ by number relative to H, and we have assumed $T_4 = 1$. Of course, if $t_{\rm ev} \geqslant t_{\rm H}$, the Hubble time at the epoch of photoevaporation, then the underlying properties of the halo, infall, ionizing source, and background Universe will evolve significantly during the process. The Hubble time at high redshift in the ΛCDM universe is

$$t_{\rm H} = \frac{2}{3H(z)} \approx 533{\rm Myr}\left(\frac{\Omega_0 h^2}{0.15}\right)^{-1/2}(1+z)_{10}^{-3/2}. \tag{25}$$

Thus, the ratio of the two time-scales is

$$\frac{t_{\rm sc}}{t_{\rm H}} = 0.184(M_7)^{1/3}\left(\frac{\Omega_0 h^2}{0.15}\right)^{1/6}(1+z)_{10}^{1/2}. \tag{26}$$

We see that this ratio is only weakly dependent on the background cosmology, and suggests that the photoevaporation of a minihalo over the range of mass and epochs of interest will be completed in less than a Hubble time, if this estimate of $t_{\rm ev}$ is correct.

2.5 Ionizing photon consumption

An important quantity characterizing the effect of minihaloes on the process of reionization is the consumption of ionizing photons which results from photoabsorption by minihalo atoms during their photoevaporation. We can parametrize this consumption by the photon-to-atom ratio, $\xi \equiv N_\gamma/N_{\rm a}$, i.e. how many photons per minihalo atom are required to photoevaporate the halo. Collapsed minihaloes are significantly denser than the IGM, thus the recombination rate inside is significantly higher, leading to a much higher photon consumption rate per unit time per atom, which could in turn have a substantial effect on the progress and duration of reionization.

We define the effective absorption cross-section at frequency ν of a minihalo at a given time t as

$$\sigma_{{\rm eff},\nu}(t) \equiv \int_0^\infty 2\pi r \left[1 - {\rm e}^{-\tau_\nu(r,t)}\right]\, {\rm d}r, \tag{27}$$

where $\tau_\nu = \tau_{\nu,{\rm H}} + \tau_{\nu,{\rm He\,I}} + \tau_{\nu,{\rm He\,II}}$ is the total bound–free opacity at impact parameter r and time t, including the minihalo gas which is leaving the halo in a wind, where

$$\tau_{\nu,i}(r,t) = \int_{x_{\rm min}}^{x_{\rm max}} \sigma_{{\rm bf},i}(\nu) n_i\, {\rm d}x, \tag{28}$$

where $\sigma_{{\rm bf},i}$ is the bound–free cross-section, $x_{\rm min}$ and $x_{\rm max}$ are the positions of the Lagrangian boundary of the original halo material at this impact parameter, and n_i is the number density for species i. The number of photons absorbed by the minihalo gas per minihalo atom over time $t_{\rm ev}$ is then given by

$$\xi_\tau = \frac{1}{N_{\rm a}} \int_0^{t_{\rm ev}} \int_{\nu_{\rm th,\,H}}^\infty F_\nu(t)\sigma_{{\rm eff},\nu}(t)\, {\rm d}\nu\, {\rm d}t, \tag{29}$$

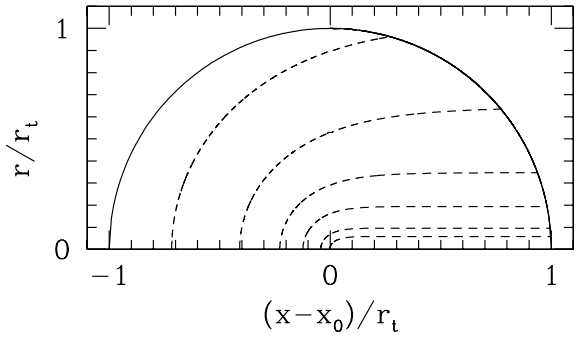

Figure 3. The ISL shape inside a minihalo (the halo boundary is indicated by the solid line), according to the ISL approximation for $\chi/\chi_{S,0} = 0.01$, 0.1, 1, 10, 100 and 250 (dashed-line curves from left to right). x_0 is the position of the centre of the halo along the x-axis. Both the impact parameter r and axis coordinate $x - x_0$ are in units of the halo radius r_t. The source is located outside the box, to the left, at $x = 0$, where $x_0 \gg r_t$. We assume $T_4 = 2$.

where $\nu_{\rm th,H}$ is the ionization threshold frequency for hydrogen and $F_\nu(t)$ is the time-dependent ionizing photon flux per unit frequency.

Alternatively, ξ can be calculated from the direct count of the number of ionizations experienced per initial minihalo atom, by using the recombination rate, according to

$$\xi_{\rm rec} = 1 + \frac{1}{N_{\rm a}} \int_0^{t_{\rm ev}} {\rm d}t \int {\rm d}V \left(\alpha_{\rm H}^{(2)} n_{\rm e} n_{\rm HII} + \alpha_{\rm He}^{(2)} n_{\rm e} n_{\rm HeII}\right), \tag{30}$$

where $n_{\rm e}$ is the number density of electrons, $n_{\rm HII}$ and $n_{\rm He\,II}$ are the number densities of H II and He II, and $\alpha_{\rm H}^{(2)}$ and $\alpha_{\rm He}^{(2)}$ are the case B recombination coefficients for H II and He II, respectively, and the volume integral is over all Lagrangian fluid elements initially inside the minihalo when the I-front first encountered it. We have neglected the recombinations of He III to He II because these generally contribute diffuse flux which is absorbed on-the-spot by H and He.

A naïve estimate of ξ is obtained just by counting the recombinations per minihalo atom per evaporation time under the simplifying assumptions that the minihalo is optically thin, instantaneously ionized and remains static for a time $t_{\rm sc}$. In that case, if we ignore the contribution of He to recombinations, equation (30) yields this optically thin, static (OTS) approximation for ξ, according to

$$\xi_{\rm OTS} = f \frac{C_{\rm int} \langle n_{\rm H} \rangle \alpha_{\rm H}^{(2)}}{1 + \delta_{\rm TIS}} t_{\rm sc}, \tag{31}$$

where $\langle n_{\rm H} \rangle$ is the mean H atom number density inside a halo, $C_{\rm int} \equiv \langle n_{\rm H}^2 \rangle / \langle n_{\rm H} \rangle^2 = 444^2$ and $1 + \delta_{\rm TIS} = 130.6$ are the effective clumping factor and average overdensity, respectively, of a TIS halo, as measured with respect to the cosmic mean background density, and f is an 'efficiency' factor which is intended to correct the optically thin, static minihalo estimate for the effects of gas dynamics, to be derived from numerical simulations (Haiman et al. 2001). Combining equations (24) and (31), this yields

$$\xi_{\rm OTS} = 206 f T_4^{-3/4} M_7^{1/3} \left(\frac{\Omega_0 h^2}{0.15}\right)^{-1/3} (1+z)_{10}^{-1}. \tag{32}$$

According to this estimate, if $f \approx 1$ as claimed by Haiman et al. (2001), based on their simulation of a uniformly ionized minihalo with zero optical depth, the photoevaporation of minihaloes can be an enormous sink of ionizing photons during the reionization epoch. By contrast, atoms in the IGM at closer to the mean baryon density have otherwise been estimated previously to consume only $\xi \sim 1$ photons per atom during reionization (Gnedin 2000a; Miralda-Escude, Haehnelt & Rees 2000). It is crucial, therefore, for us to perform the detailed simulations reported here in order to derive the efficiency factor f in equation (32) properly.

3 THE CALCULATION

3.1 Basic equations

3.1.1 Gas dynamical conservation equations

We solve the Eulerian conservation equations of fluid dynamics for the vector $\boldsymbol{U}$ of the densities of conserved quantities in 2D, cylindrical symmetry,

$$\boldsymbol{U} = (\rho, \rho v_x, \rho v_r, E, n_{i,z}), \tag{33}$$

with mass density ρ, momentum densities ρv_x in the x-direction and ρv_r in the radial direction, energy density $E = \rho(v_x^2 + v_r^2)/2 + \epsilon$ and number density of chemical species i in ionization stage z, $n_{i,z}$. Here v_x and v_r are the velocity components, $\epsilon = c_V T$ is the specific internal energy, T is the temperature and c_V is the isochoric specific heat. The Eulerian conservation equations can then be written as

$$\frac{\partial \boldsymbol{U}}{\partial t} + \frac{\partial \boldsymbol{F}(\boldsymbol{U})}{\partial x} + \frac{\partial \boldsymbol{G}(\boldsymbol{U})}{\partial r} = \boldsymbol{S}, \tag{34}$$

where $\boldsymbol{F}(\boldsymbol{U})$ and $\boldsymbol{G}(\boldsymbol{U})$ are the fluxes of $\boldsymbol{U}$ in the x- and r-directions, respectively, given by

$$\boldsymbol{F}(\boldsymbol{U}) = \left[\rho v_x, \rho v_x^2 + p, \rho v_x v_r, v_x(E+p), n_{i,z} v_x\right], \tag{35}$$

and

$$\boldsymbol{G}(\boldsymbol{U}) = \left[\rho v_r, \rho v_x v_r, \rho v_r^2 + p, v_r(E+p), n_{i,z} v_r\right], \tag{36}$$

and $\boldsymbol{S}$ are the source terms

$$\begin{aligned} \boldsymbol{S} = \Bigg[& -\frac{\rho v_r}{r}, -\frac{\rho v_x v_r}{r} - (\nabla\phi)_x, -\frac{\rho v_r^2}{r} - (\nabla\phi)_r, \\ & -\frac{v_r(E+p)}{r} - \boldsymbol{v}\cdot\nabla\phi - \Lambda + \Gamma, -\frac{n_{i,z} v_r}{r} + S_{i,z} \Bigg]. \end{aligned} \tag{37}$$

Here p is the pressure, ϕ is the gravitational potential, Λ is the cooling rate, Γ is the heating rate, and $S_{i,z}$ is the source function for the chemical species i in ionization stage z, as described in Section 3.1.2. We use the ideal gas equation of state for a monatomic gas ($\gamma = 5/3$)

$$p = (\gamma - 1)\epsilon\rho. \tag{38}$$

3.1.2 Non-equilibrium chemical reaction network

We take account of the non-equilibrium ionization balance of H, He, and a possible admixture of heavy elements C, N, O, Ne, and S, as described in Raga, Mellema & Lundquist (1997), Mellema et al. (1998), and references therein. [For a description of the details and checks of our microphysics, the reader is referred to Mellema (1993)].

The source function for the non-equilibrium chemical reaction network is given by

$$\begin{aligned} S_i = {} & n_{\rm e} n_{i,z+1} \alpha_{i,z+1}(T) + n_{\rm e} n_{i,z-1} C_{i,z-1} - n_{\rm e} n_z \alpha_{i,z}(T) \\ & - n_{\rm e} n_{i,z} C_{i,z} + n_{i,z-1}\phi_{i,z-1} - n_{i,z}\phi_{i,z}, \end{aligned} \tag{39}$$

where, as above, i labels the chemical elements, z labels the ionization state, $\alpha_{i,z+1}(T)$ is the recombination rate from stage $z+1$ to z, $C_{i,z-1}$ is the collisional ionization rate from $z-1$ to z, $\phi_{i,z} = \int_{\nu_{{\rm th},i}}^{\infty} (F_\nu \sigma_{\nu,i,z})/(h\nu) {\rm d}\nu$ is the photoionization rate from z to $z+1$, and $\nu_{{\rm th},i}$ is the photoionization threshold for species i. Charge exchange reactions are included, although we have not displayed them in equation (39). Recombination rates include radiative and dielectronic rates.

The electron number density $n_{\rm e}$ is given by $n_{\rm e} = n_{\rm HII} + n_{\rm He\,II} + 2n_{\rm He\,III} + n_{\rm C}$. The contribution of one electron per carbon atom is added to ensure that the electron number density is always positive. Since the ionization threshold of carbon is below 13.6 eV and the IGM is transparent to these photons even before reionization, C is always at least singly ionized. The contribution of the other metals to the electron density is assumed negligible.

3.1.3 Radiative cooling and photoheating

Our non-equilibrium cooling function includes collisional line excitation and ionization, recombination and free–free cooling due to H, C, N, O, Ne, and S, as described and tested in detail in Raga

et al. (1997), to which we have added He cooling and the Compton cooling which results from inverse Compton scattering of the CMB photons off free electrons. The Compton cooling rate is given by

$$\Lambda_{\rm Comp} = 5.65 \times 10^{-36} n_{\rm e}(1+z)^4(T - T_{\rm CMB})\,{\rm erg\,cm^{-3}\,s^{-1}} \qquad (40)$$

(Shapiro & Kang 1987), where $T_{\rm CMB} = 2.73(1+z)$ is the CMB temperature at redshift z, $n_{\rm e}$ is the local density of free electrons, and T is the local gas temperature.

The photoheating rate Γ (in units of erg cm^{-3} s^{-1}) is the sum of the ionization heating terms for each of the species H I, He I, and He II:

$$\Gamma_{i,z} = n_{i,z}\int_{\nu_{{\rm th},i,z}}^{\infty} \frac{F_\nu(h\nu - h\nu_{{\rm th},i,z})}{h\nu}\sigma_{{\rm bf},\nu,i,z}\,{\rm d}\nu. \qquad (41)$$

3.1.4 Radiative transfer and the ionizing flux

The energy flux of ionizing photons at a point with coordinates (r, x) for a source on the x-axis at position x_0 is given by

$$F_\nu(r,x) = \frac{L_\nu}{4\pi\left[r^2 + (x-x_0)^2\right]}{\rm e}^{-\tau_\nu(r,x)}. \qquad (42)$$

Here L_ν is the source luminosity at frequency ν, and $\tau_\nu(r, x)$ is the bound–free optical depth from the source to the point (r, x), given by

$$\tau_\nu(r,x) = \sigma_{\nu,{\rm H\,I}}N_{\rm H\,I} + \sigma_{\nu,{\rm He\,I}}N_{\rm He\,I} + \sigma_{\nu,{\rm He\,II}}N_{\rm He\,II}, \qquad (43)$$

where $N_{i,z}$ is the column density of species i at ionization stage z along the line from the source to the point (r, x).

3.1.5 Gravity force

We have modified the code to include the gravity field due to the halo of dark matter and gas, and the infalling matter, as discussed in detail in Appendix A. We neglected the small change in this gravity force over time which results from the gas dynamical evolution which moves the gas relative to the dark matter. Thus the density field used for the gravity calculation is spherically symmetric at all times and the gravitational acceleration is given by

$$a_{\rm grav} = -\nabla\phi = \frac{GM(\leqslant R)}{R^2}, \qquad (44)$$

where $M(\leqslant R)$ is the time-varying mass within the spherical radius $R = (r^2 + x^2)^{1/2}$. This force is included in the Euler equations (34) through the source term $\boldsymbol{S}$ as shown in equation (37).

3.2 Initial conditions

3.2.1 Minihalo and cosmological infall

As discussed above, the halo in our illustrative simulations has radius $r_t = 0.76$ kpc, and virial temperature $T_{\rm vir} = 4000$ K, corresponding to dark-matter velocity dispersion $\sigma_V = 5.2$ km s^{-1}. The initial number density and velocity profiles of the halo and the infall are shown in Fig. 4. For comparison with our simulation results at later times, we show the initial conditions on the computational grid in Fig. 5 (top to bottom): (1) the density contours (logarithmically spaced), (2) the initial velocity field, and cuts along the axis of: (3) gas number density n, (4) velocity v_x, and (5) isothermal Mach number $M_{\rm I} \equiv v/c_{\rm s,I}$, where $c_{\rm s,I}$ is the isothermal sound speed. The computational box is chosen so that the turn-around radius of the cosmological infall starts well inside the box. This ensures that the gas next to the simulation boundaries (excluding the axis of symmetry) is outflowing throughout the simulation, consistent with our transmissive numerical boundary conditions (see Section 4).

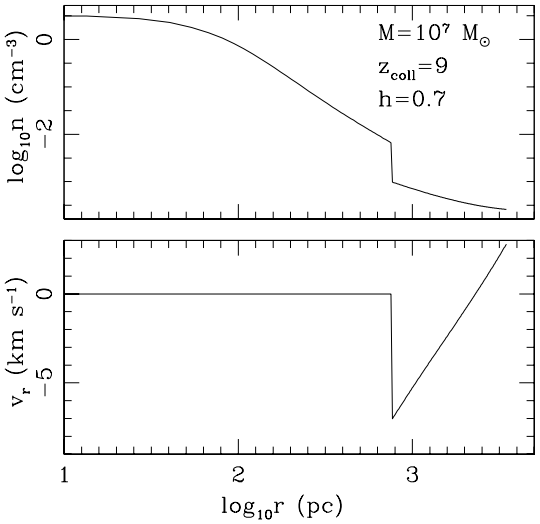

Figure 4. Initial conditions for the minihalo photoevaporation simulations (TIS halo + self-similar cosmological infall): atomic number density (upper panel), and radial velocity (lower panel) profiles versus radius for minihalo of mass $M_7 = 1$ at $(1+z)_{10} = 1$.

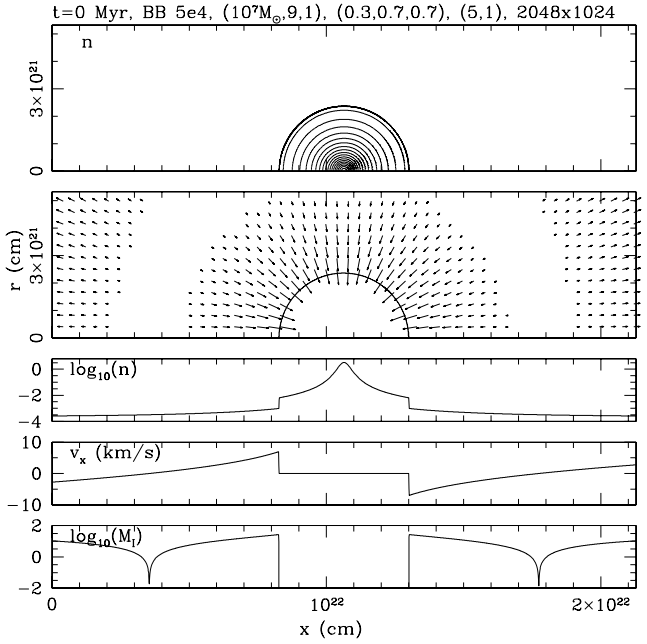

Figure 5. Initial time-slice at $t = 0$ Myr ($z = 9$ in a ΛCDM universe), from top to bottom: (1) isocontours of atomic density, logarithmically spaced, in (r, x)-plane of cylindrical coordinates; (2) flow velocities; arrows are plotted with length proportional to gas velocity. An arrow of length equal to the spacing between arrows has velocity 5 km s^{-1}; the minimum velocities plotted are 1 km s^{-1}. The solid line indicates the boundary of the minihalo; cuts along the $r = 0$ axis of: (3) gas number density n, (4) velocity v_x, and (5) isothermal Mach number $M_{\rm I}$. The source is located outside the box, far to the left along the x-axis. The label on top shows the snapshot time, source spectrum, halo parameters and flux level $(M, z_{\rm coll}, F_0)$, cosmological parameters, (Ω_0, λ_0, h), spacing of velocity arrows and minimum velocity, $(v_{\rm max}, v_{\rm min})$, and finest-grid resolution.

3.2.2 Source spectra and evolution

The source is on the axis of symmetry, far away (thus the rays are close to parallel, although the code actually takes the true angles properly into account) to the left of the box. We consider three possible spectra as described in Section 1: two stellar cases, blackbody spectra with effective temperatures $T = 50\,000$ K ('BB 5e4') for Population II stars and $T = 10^5$ K ('BB 1e5') for Population III stars, and a power-law QSO-like energy spectrum with index $\alpha = -1.8$. As the Universe expands, the proper distance between the source and the minihalo grows, as $x_0(t) \propto a(t)$, where $a(t)$ is the cosmic scale factor, so the incident flux level decreases $\propto x_0^{-2} \propto a(t)^{-2}$. In principle, the clustering of haloes caused by structure formation might keep the proper separation of the source and minihalo from increasing as fast as we have assumed. In practice, however, for all cases considered here, the evaporation times are smaller than a Hubble time, so the time-dependence of the source–minihalo separation distance is a minor effect.

We have assumed here that the source luminosity is steady throughout the evaporation time. This allows us to compare effects of sources with different spectra on an equal footing, while also providing a standard of comparison for future simulations which will consider time-varying source luminosities.

3.2.3 When the R-type I-front encounters the simulation volume at $t = 0$

The I-front has a finite width of ∼(10–20) mean free paths. For the intergalactic weak, R-type I-front which encounters the minihalo, this mean free path in the IGM is a few kpc, which is similar to our simulation box size. Therefore, it would be inaccurate to start the simulations by assuming a sharp I-front at the left box boundary. Instead, we start our simulations shortly before the I-front arrival at the left boundary, as follows. We assume that the gas outside the box is uniform, at the mean IGM density, for which case there is an exact solution for the weak, R-type I-front propagation. We then use the frequency-dependent optical depths given by the current position of the I-front obtained from the analytical solution to attenuate the spectrum of the photoionizing source which enters the computational box. While not exact (e.g. due to infall which slightly increases the local density around the halo) this approach closely imitates the gradual rise in the photoionizing radiation flux arriving from the source as the I-front approaches and the hardening of the spectrum due to the deeper penetration of higher-energy photons. As an alternative, it is also possible to take a much larger simulation box, which would allow the I-front to relax to its correct structure before arriving at the halo. However, such an approach would either degrade the resolution unacceptably, or else the simulation would become prohibitively (and needlessly) more expensive.

4 NUMERICAL METHOD AND TESTS

4.1 The method

We use a 2D axisymmetric adaptive mesh refinement (AMR) code (called CORAL) described in detail in Raga et al. (1995) and Mellema et al. (1998). The code has been extensively tested and applied to a range of problems including simulations of Herbig–Haro jets and the photoevaporation of uniform density interstellar clouds near planetary nebulae. Here we will discuss the numerical details of the code only briefly, concentrating on the new elements in the code introduced by us, and we refer the reader to these earlier papers and references below for a more in-depth discussion.

The numerical scheme for solving the Euler equations is an adaptive grid implementation of the van Leer flux vector splitting method (van Leer 1982), improved to second-order accuracy by use of linear gradients within cells as described in Arthur (1991). The refinement and de-refinement criteria are based on the gradients of all code variables. When the gradient of any variable is larger than a pre-defined value the cell is refined, while when the criterion for refinement is not met the cell is de-refined. We have modified the code to include the gravitational acceleration in equation (44), as discussed in detail in Appendix A. We impose reflective boundary conditions on the axis and transmissive boundary conditions on the other three boundaries of the box.

The code time-step is set in general by the minimum of the time-steps determined by the Courant condition, the ionization time-scale and gravity,

$$\Delta t = \min(\epsilon_{\rm Cour}\Delta t_{\rm Cour}, \epsilon_{\rm ion}\Delta t_{\rm ion}, \epsilon_{\rm grav}\Delta t_{\rm grav}). \quad (45)$$

The Courant time in equation (45) is

$$\Delta t_{\rm Cour} = \Delta x / c_{\rm s}, \quad (46)$$

where Δx is the cell width. The ionization time-scale here is that for ionizing hydrogen,

$$\Delta t_{\rm ion} = \epsilon_{\rm ion}\frac{n_{\rm H\,I}}{({\rm d}n_{\rm H\,I}/{\rm d}t)} = \epsilon_{\rm ion}\frac{n_{\rm H\,I}}{|n_{\rm H\,I}\phi_{\rm H\,I} - n_{\rm H\,II}^2\alpha_{\rm H}^{(2)}|}, \quad (47)$$

where $\phi_{\rm HI}$ is the photoionization rate for hydrogen, $n_{\rm HI}$ and $n_{\rm HII}$ are the number densities of neutral and ionized hydrogen, $\alpha_{\rm H}^{(2)}$ is the case B recombination coefficient for hydrogen, and $\epsilon_{\rm ion}$ is a constant to be determined. The gravity time is just

$$\Delta t_{\rm grav} = (\Delta x / a_{\rm grav})^{1/2}. \quad (48)$$

The constants ϵ_i are small numbers whose values are chosen to ensure accuracy and stability while minimizing the total number of time-steps per simulation. In all cases considered here, the time-step is set by the Courant condition, except when the fast, R-type I-front propagates through the computational box. In the latter case, the ionization time-scale is smaller than the Courant time, and the value of $\epsilon_{\rm ion}$ is chosen by experimentation to optimize the accuracy and efficiency of the test problem described in Section 4.3. For the Courant condition, the van Leer flux vector splitting scheme is stable when $\epsilon_{\rm Cour} \leqslant [2\gamma + M(3-\gamma)]/(\gamma+3)$, where $\gamma = 5/3$ is the adiabatic index and M is the Mach number. For $M = 0$ we obtain the condition $\epsilon_{\rm Cour} \leqslant 5/7$ for the scheme to be stable for any Mach number M. For the current simulations we utilized the conservative value $\epsilon_{\rm Cour} = 0.4$.

The microphysical processes – chemical reactions, radiative processes, transfer of radiation, heating and cooling – are implemented though the standard approach of operator-splitting (i.e. solved each time-step, side-by-side with the hydrodynamics and coupled to it through the energy equation). The energy and chemical rate equations are solved semi-implicitly. We follow the non-equilibrium evolution of the ionic species of H, He, C II–VI, N I–VI, O I–VI, Ne I– VI and S II–VI. The species C I and S I are assumed to be fully ionized since their ionization thresholds are below the ionization threshold of hydrogen and the gas is largely optically thin to such low-energy photons [for details see Mellema et al. (1998) and references therein]. The method for solving the non-equilibrium chemistry equations is from Schmidt-Voigt & Koeppen (1987) and is implemented as described and tested in Raga et al. (1997) and Mellema et al. (1998). We use case B recombination coefficients

and the corresponding cooling rates, as is appropriate for the range of densities and temperatures in these simulations.

Radiative transfer of the ionizing photons is treated explicitly by taking into account the bound–free opacity of H and He in the photoionization rates and heating rates as explained in detail in Mellema et al. (1998). In order to speed up the radiative transfer calculation, the optical depths are approximated as described in Tenorio-Tagle, Bodenheimer & Noriega-Crespo (1983), as follows:

$$\tau_\nu = \begin{cases} \tau_{\nu,A} \text{ for } \nu_{\rm th,HI} \leqslant \nu \leqslant \nu_{\rm th,HeI} \\ \tau_{\nu,B} \text{ for } \nu_{\rm th,HeI} \leqslant \nu \leqslant \nu_{\rm th,HeII} \\ \tau_{\nu,C} \text{ for } \nu_{\rm th,HeII} \leqslant \nu, \end{cases} \quad (49)$$

where

$$\tau_{\nu,A} = \tau_{\nu,\rm HI}\left(\frac{\nu}{\nu_{\rm th,HI}}\right)^{-2.8}, \quad (50)$$

$$\tau_{\nu,B} = \left[(0.63)^{1.7}\tau_{\nu,\rm H\,I} + (1.81)^{1.7}\tau_{\nu,\rm He\,I}\right]\left(\frac{\nu}{\nu_{\rm th,HI}}\right)^{-1.7}, \quad (51)$$

and

$$\tau_{\nu,C} = \left[\tau_{\nu,\rm H\,I} + (2.73)^{2.8}\tau_{\nu,\rm He\,I} + 4^{2.8}\tau_{\nu,\rm He\,II}\right]\left(\frac{\nu}{\nu_{\rm th,HI}}\right)^{-2.8}. \quad (52)$$

Here $\tau_{\nu,i,z} = \sigma_{{\rm bf},\nu,i,z}N_i$ are the optical depths at the respective ionization thresholds of H I, He I and He II. This allows us to precompute the integrals over frequency involved in calculating photoionization and photoheating rates for each assumed source spectrum to make an extensive look-up table for these rates as functions of the threshold optical depths, for use in the rapid computation of these rates during each run by interpolation between entries in the look-up table. In order to speed up the calculations further, the optical depths are normally recalculated once every five time-steps.

4.2 Simulation parameters

Our box size in (r, x) dimensions is 3.45×6.9 kpc^2, except for the uniform IGM simulations in Sections 4.3 and 5.1, where we adopted larger boxes, as described there. The resolution at the finest grid level (i.e. fully refined) is 1024×2048 cells, again with the exception of the simulations in Sections 4.3 and 5.1, where such high resolution was not required, but a longer propagation time was necessary, so we used resolutions of 64×8192 and 512×1024, respectively.

The gas consists of hydrogen and helium in primordial abundance (24.2 per cent He by mass), with a small trace of metals (C, N, O, Ne and S) at 10^{-3} Z$_\odot$. The initial ionizing flux we adopt is $F_0 = 1$, except in Section 4.3 where we use $F_0 = 4$. Each photoevaporation simulation took from several days to 1 week on a 2 GHz Athlon processor.

4.3 Test problem: R-type I-front in uniform IGM

In order to track properly the supersonic, weak, R-type I-fronts which sweep into and around our minihaloes, we defined an 'ionization time-step' related to the time-scale for ionizing hydrogen, as described above in Section 4.1. We tested the scheme and adjusted the value of $\epsilon_{\rm ion}$ by performing a simulation of an ionization front propagating through a uniform-density IGM in a long and thin (44 kpc $\times$ 5.64 Mpc), quasi-1D simulation box at resolution 64×8192. In this case, the gas is pure hydrogen, so there is a well-known exact analytical solution for the I-front propagation (Shapiro & Giroux 1987). The density of the gas is equal to the mean cosmic baryon density at $z = 9$. The source is located on the symmetry axis, 0.5 Mpc to the left of the computational box, with a flux as measured at the left boundary of the box equal to $F_0 = 4$. At time $t = 0$, the box is neutral. We identify the location of the I-front as the position at which the ionized fraction is $x = 0.5$. The result is plotted in Fig. 6. By experiment, we found that $\epsilon_{\rm ion} = 0.05$ is sufficient to obtain the correct velocity for the R-type I-front to better than 5 per cent, as shown in Fig. 6. Using larger $\epsilon_{\rm ion}$ can lead to an underestimate of the velocity by a significant amount.

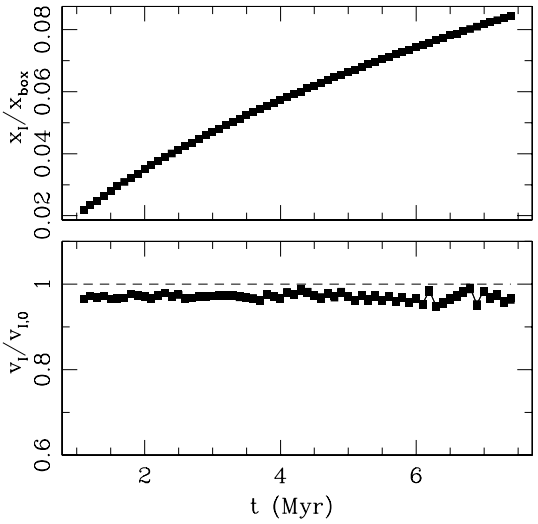

Figure 6. R-type I-front speed. Position $x_{\rm I}$ (in units of the box length $x_{\rm box} = 5.64$ Mpc; upper panel) and velocity $v_{\rm I}$ (in units of the analytical prediction as described in the text; lower panel) of an R-type ionization front propagating through the mean IGM at redshift $z = 9$.

5 RESULTS

5.1 Structure of global I-front in the IGM during reionization: the weak, R-type phase

To study the detailed temperature and ionization structure of the global I-front during reionization in its weak, R-type phase and the dependence of these on the source spectrum, we performed a set of three simulations of an I-front in the uniform IGM at $z = 9$, by 'zooming in' with a smaller box (34.5×69 kpc^2) and better length resolution (512×1024, fully refined) than were used in the test problem in the previous section. The source in each case produced a flux $F_0 = 1$ at the left boundary of the simulation box, with a different spectrum for each simulation. The results are shown in Figs 7–10. As expected, for the cases with harder spectra (i.e. QSO, BB 1e5), the I-front is broader than in the case BB 5e4, due to the more deeply penetrating hard photons of the former cases. There is significant pre-heating and pre-ionization in the former cases, ahead of the point inside the I-front at which the H neutral fraction is 0.5. In all cases, the ionization of He is predominantly from He I on the neutral side to He III on the ionized side, with only a small fraction of He II. The position of the hydrogen I-front ($x_{\rm H} = 0.5$) is nearly coincident with the corresponding point for helium ($x_{\rm He} = 0.5$) for the softer BB 5e4 spectrum, while for the harder QSO and BB 1e5 spectra the He I-front is more advanced by $\sim$7 kpc. Another important difference to note is that the post-front temperature is

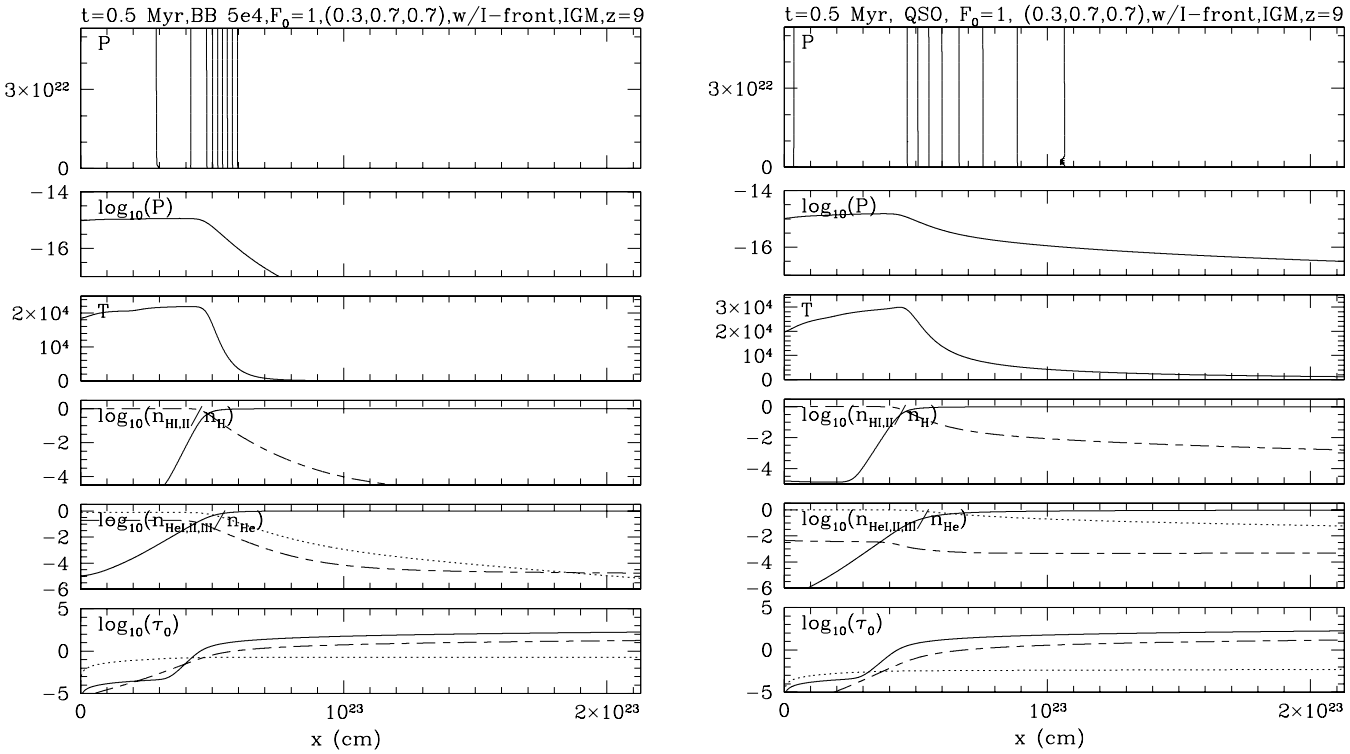

Figure 7. Detailed structure of R-type ionization front in the mean IGM at $z = 9$ at time 0.5 Myr after the ionizing flux turns on at the left-side boundary of the box. (a) (left) BB 5e4 case and (b) (right) QSO case. From top to bottom: (1) isocontours of pressure, logarithmically spaced, in (r, x)-plane of cylindrical coordinates; cuts along the x-axis (the I-front propagation direction) of (2) pressure, (3) temperature T, (4) H I (solid) and H II (dotted) fractions; (5) He I (solid), He II (dashed) and He III (dotted) fractions; (6) bound–free optical depths measured from $x = 0$ along the x-axis, for H I (solid), He I (dashed), and He II (dotted) at their respective ionization thresholds. The source is located 0.5 Mpc, to the left of the box.

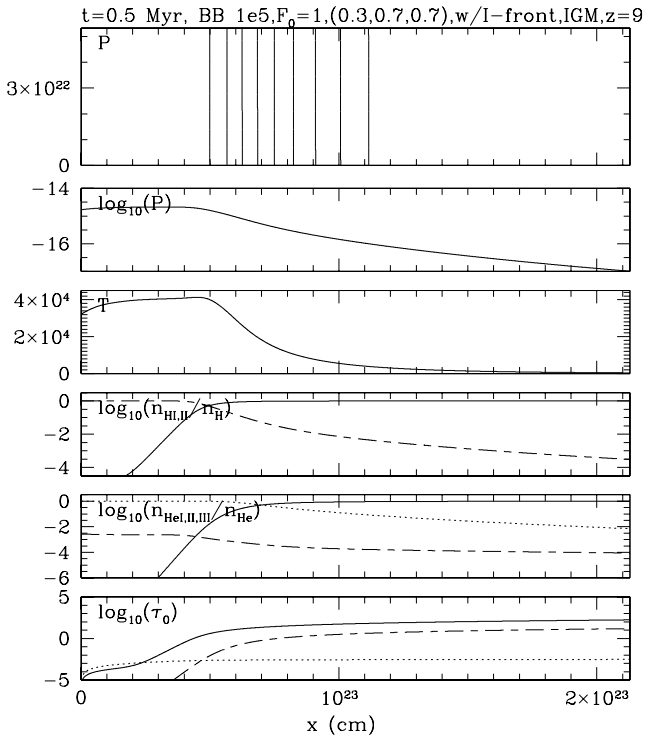

Figure 8. Same as in Fig. 7, but for the BB 1e5 case.

$\sim 2 \times 10^4$ K in the BB 5e4 case, but $\sim 3 \times 10^4$ K in the QSO case, and even higher, $\sim 4 \times 10^4$ K in the BB 1e5 case. The ionization states of the trace of heavier elements also differ significantly for different source spectra, as shown in Figs 9 and 10. The BB 5e4 spectrum ionizes C, N and O mostly to C III, N III and O III, respectively, with only small fractions, of order 10 per cent, of C IV, N IV and O IV, while the BB 1e5 spectrum ionizes these species mostly up to ionization stage IV, with a notable fraction (>10 per cent) of ionization stage V, and tiny fractions of O VI and N VI. Finally, the hard QSO spectrum is able also to produce fractions as high as a few per cent for O VI and N VI, while the bulk of the metals reside in the ionization stages IV and V.

5.2 When the I-front encounters the minihalo: weak, R-type phase inside the minihalo

As the weak, R-type I-front propagates towards the minihalo, it encounters a steeply rising density, first the infall region and then the virialized region of the minihalo, itself, and its velocity drops precipitously. Fig. 11 shows the evolution of the I-front position $x_{\rm I}$ (upper panel), its velocity $v_{\rm I}$ (middle panel) and the mass fraction $M/M_{\rm init}$ of the gas initially within the original hydrostatic sphere (bottom panel) which remains neutral over time in the BB 5e4 case. The initial speed of the I-front as it enters the box is about 10 000 km s^{-1}, dropping to $\sim$ 1000 km s^{-1} by the time the front crosses the virial radius of the halo. As a result, the I-front is initially a weak, R-type front even after it enters the minihalo. It takes about 5 Myr for the front to slow to the R-critical front speed $v_{\rm R} \cong 2c_{\rm s,I,2} \approx 20$ km s^{-1}, where the isothermal, post-front sound speed is $c_{\rm s,I,2} \cong 11$ km s^{-1},

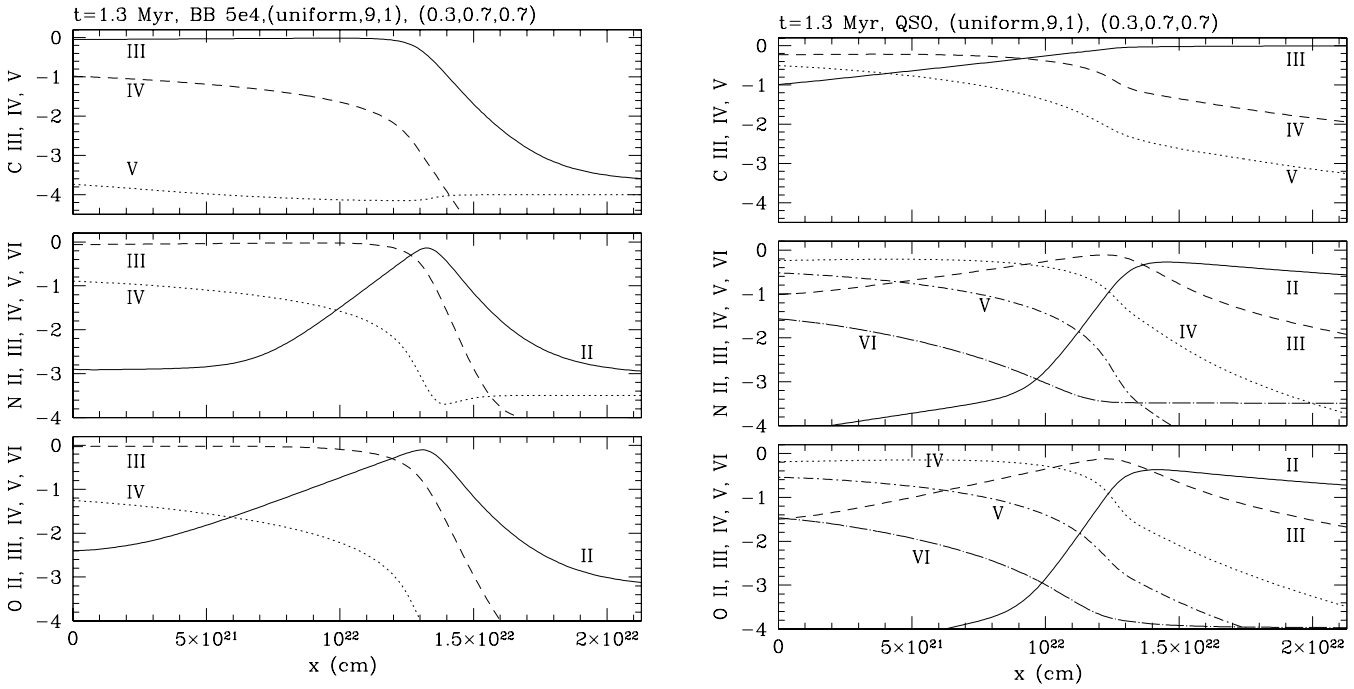

Figure 9. Ionization structure of metals in an R-type I-front propagating in the mean IGM at $z = 9$, 1.3 Myr after the front enters the box on the left-hand side. C, N and O ionic fractions along symmetry axis: (a) (left) BB 5e4 case; (b) (right) QSO case.

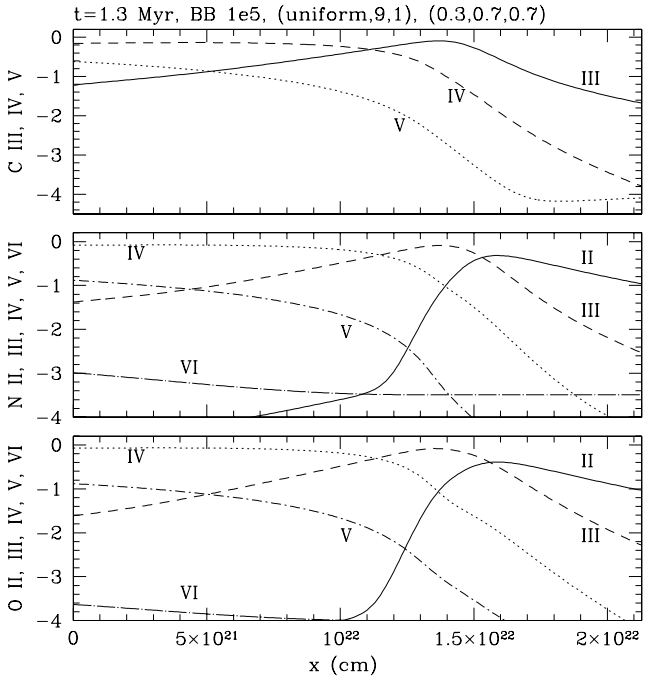

Figure 10. Same as in Fig. 9, but for the BB 1e5 case.

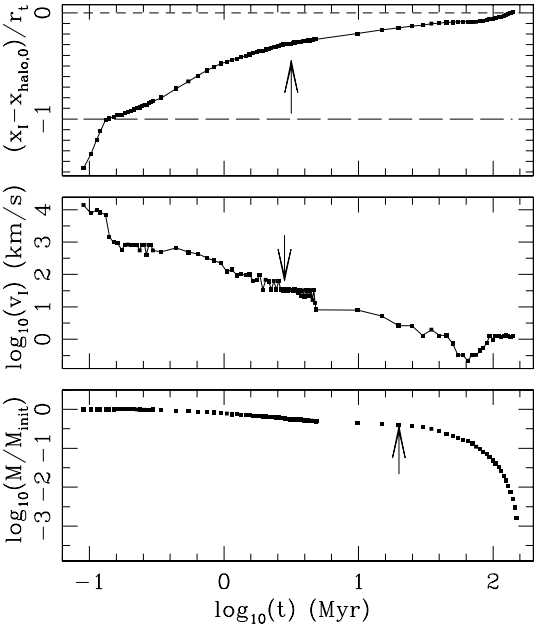

Figure 11. Evolution of the I-front from R-type to D-type inside the minihalo for the BB 5e4 case. (Upper panel) position x_I (relative to minihalo centre, in units of the minihalo radius r_t at $t = 0$) and (middle panel) velocity v_I of the I-front as it travels toward and across the minihalo. The positions of the halo boundary (long-dashed line) and centre (short-dashed line) are also indicated. (Lower panel) fraction of mass M_{init}, the mass which is initially inside the minihalo when the intergalactic I-front overtakes it, which remains neutral, versus time t. The arrows in the top and bottom panels mark the analytically calculated width of the ISL for zero impact parameter and the mass fraction inside the ISL, respectively, while the arrow on the middle panel marks the moment when the I-front becomes R-critical, defined by the condition $v_I = 2c_{s,I,2}$, the onset of transition from R-type to D-type, where $c_{s,I}$ is the isothermal sound speed of ionized, post-front gas.

marked on the plot by an arrow, after which a compressive shock must form to lead the I-front and further decelerate it, so as to transform it to a D-type front. On the top panel, we have indicated (by another arrow) the position of the inverse Strömgren surface at zero impact parameter, as calculated in Section 2.3. The two arrows almost coincide, confirming our expectations of approximate

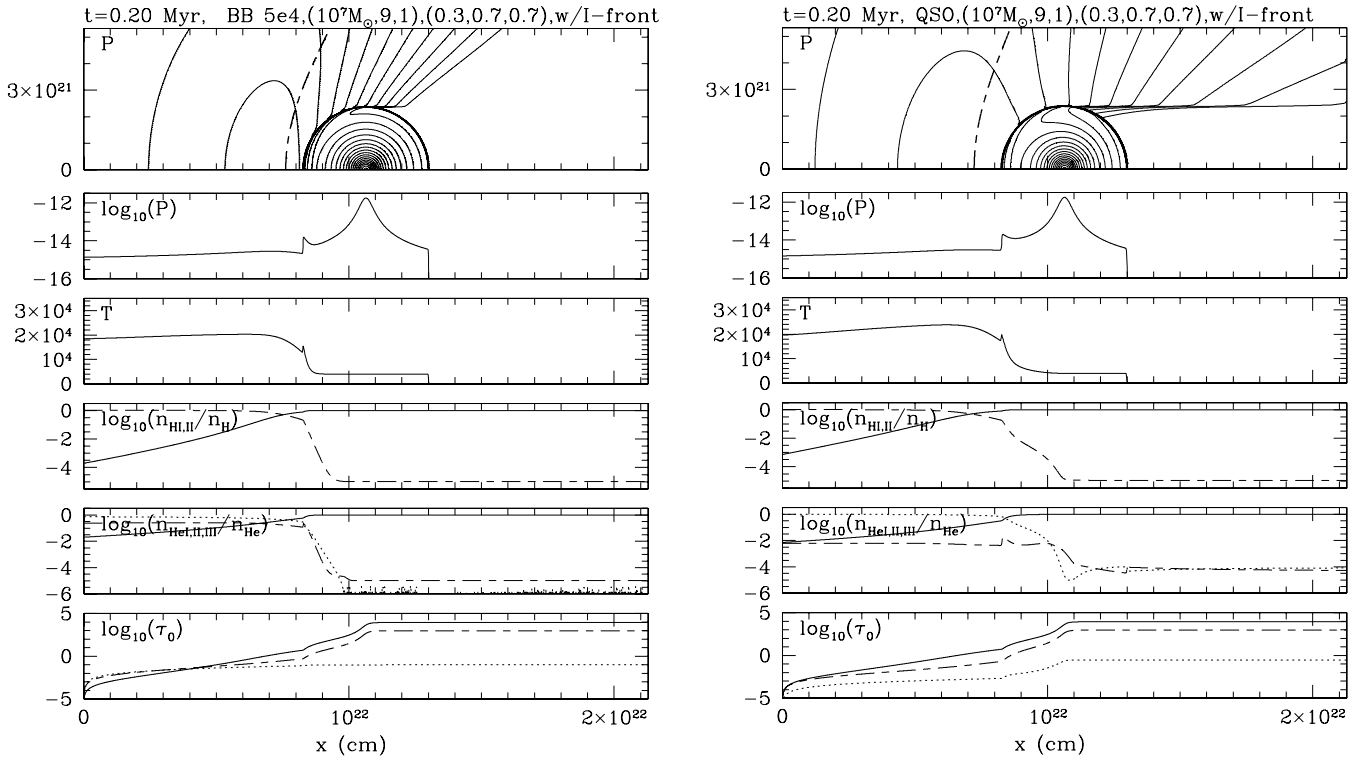

Figure 12. Weak, R-type phase of the I-front in the IGM just about to overtake a 10^7 $M_\odot$ minihalo at $z = 9$, $t = 0.2$ Myr after the I-front entered the box at the left-hand side (the ionizing source is located far to the left of computational box along the x-axis): (a) (left) BB 5e4 case and (b) (right) QSO case. Panels show the same quantities as in Fig. 7. The current position of the I-front (50 per cent ionization level of hydrogen) is indicated on the uppermost panel with the dashed line.

correspondence between the ISL (in the static analytical calculation) and the surface on which the I-front is R-critical, close to the moment of conversion of the I-front to D-type (also indicated in Fig. 2). This correspondence is not perfect, however, due to the significant approximations made in the ISL calculation. For example, due to the centrally concentrated halo density profile the I-front transition to D-type occurs in fact at different times for each impact parameter, leading to a continuously evolving I-front shape different from the shapes shown in Fig. 3.

Figs 12 and 13 show the time-slice at 0.2 Myr, shortly before the weak, R-type I-front enters the minihalo. The instantaneous position of the I-front is indicated on the top panel which shows the contours of pressure. The I-front moves faster further away from the halo due to the lower density in the infall profile and has already significantly slowed down closer to the axis. The harder photons clearly penetrate significantly deeper in the QSO and BB 1e5 cases and the halo shadow is already clearly outlined at that time by the pressure contours, even though the front itself has not yet passed the halo. These same hard photons also start to heat the halo on the source side, while deeper into the halo and in the shadow region behind it virtually no photons can penetrate due to the extremely high optical depth, $\tau \sim 10^4$ (bottom panels). While the shadow is mostly neutral in all cases, the QSO case produces a 10^{-4} fraction of He II and He III there.

In Figs 14–17 we show the structure of the flow at $t = 2.5$ Myr, when the I-front is inside the minihalo but is still a weak, R-type front, before much hydrodynamical back-reaction has begun. Figs 14 and 15 show that the gas which was initially infalling on the source side next to the halo is already reversing its velocity, however, and starting to form a shock which will sweep the IGM

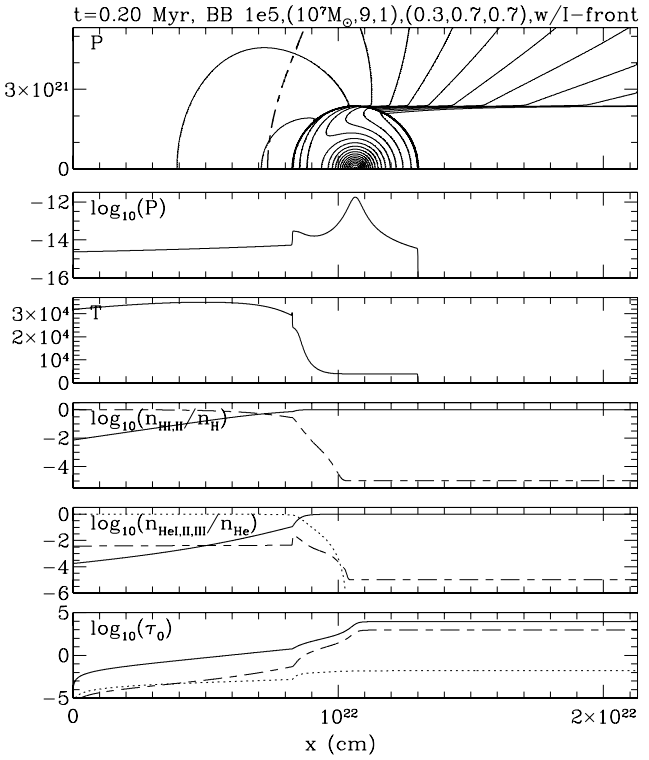

Figure 13. Same as in Fig. 12, but for the BB 1e5 case.

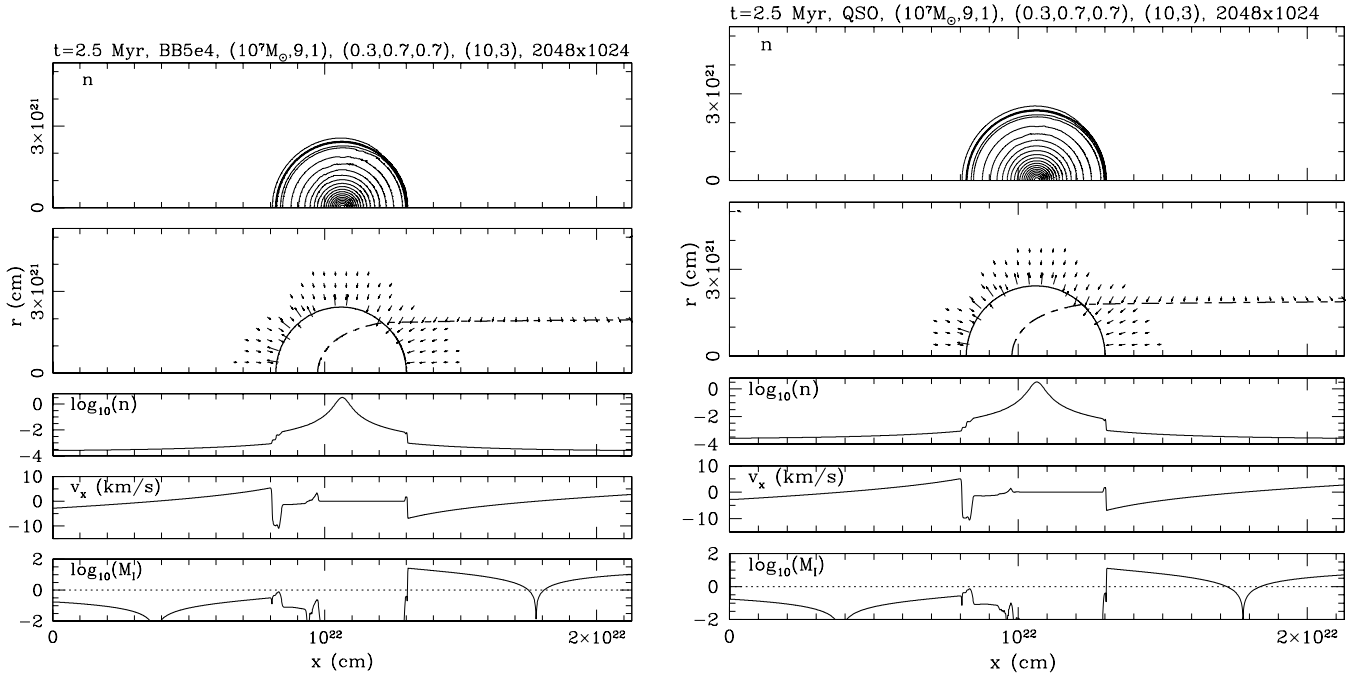

Figure 14. Weak, R-type phase of I-front inside the minihalo. Same as in Fig. 5, but for later time-slice, $t = 2.5$ Myr after I-front enters the box: (a) (left) BB 5e4 case and (b) (right) QSO case. A velocity arrow of length equal to the spacing between the arrows has velocity 10 km s^{-1}; minimum velocities plotted are 3 km s^{-1}. The solid line shows the current extent of gas initially inside the minihalo at $z = 9$. The dashed line indicates the current position of the I-front (50 per cent H-ionization contour).

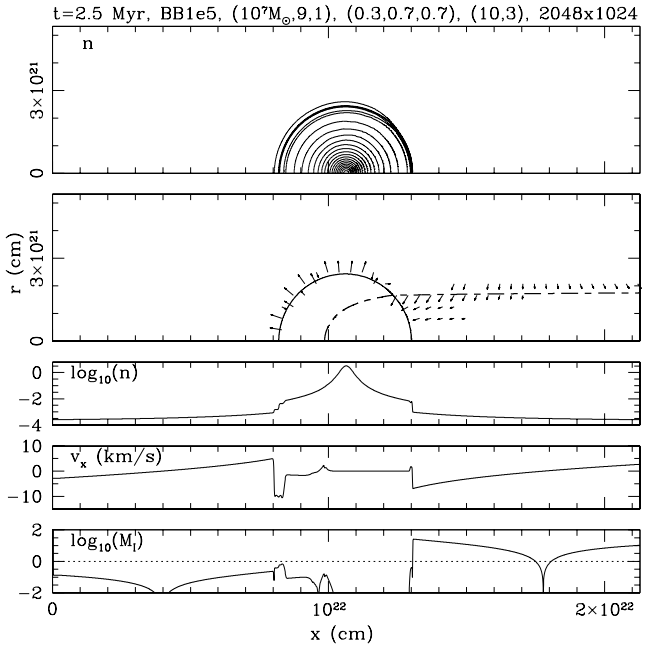

Figure 15. Same as in Fig. 14, but for the BB 1e5 case.

outward. On the other hand, on the shadow side of the halo, the gas infall continues uninterrupted. Also evident is some squeezing of the gas in the shadow due to the much higher pressure of the ionized gas outside it after the passage of the fast R-type I-front there.

5.3 I-front trapping: R-critical phase and the transition from R-type to D-type

The I-front finally slows to become an R-critical front by 5 Myr. We show the results for this time-slice for all three source spectra in Figs 18–22. To illustrate clearly that this is the R-critical phase, we focus on the Population II stellar case BB 5e4 in Fig. 18 and 'zoom in' on the region around the I-front along the x-axis in Fig. 19. All of the important properties of an R-critical I-front are evident in Fig. 19. The I-front velocity at this epoch is $v_{\rm I} \approx 16$ km s^{-1} which is not far from the estimated R-critical value of $v_{\rm R} \approx 20$ km s^{-1}, calculated based upon the immediate post-front temperature of $T_2 \approx 10\,000$ K, the pre-front $T_1 = 4000$ K (i.e. the neutral side is undisturbed minihalo gas at this virial T), $\mu_1 = 1.11$ (i.e. 90 per cent neutral), and $\mu_2 = 0.63$ (i.e. 90 per cent ionized H), which yield the post-front and pre-front isothermal sound speeds $c_{\rm s,I,2} = 11$ km s^{-1} and $c_{\rm s,I,1} = 5.3$ km s^{-1}, respectively. The numerical results show the predicted jump in density by a factor of close to 2 across the R-critical I-front, required by the I-front jump conditions. In addition, in the laboratory frame in which the neutral minihalo gas on the pre-front side is at rest (i.e. the frame in which we have plotted velocity and isothermal Mach number in Figs 18 and 19), the ionized gas just behind the front should be moving toward the neutral side at the isothermal sound speed of the ionized post-front gas, or about 11 km s^{-1}, which our plots confirm (i.e. note that the isothermal Mach number is $M_{\rm I} = 1$ at that point in the lower panel of Fig. 19). It is interesting to note that, while the gas on the ionized side of the I-front is generally optically thin during most of the evolution, the optical depth is not negligible at $t = 5$ Myr. According to Fig. 19, the H optical depth across the ionized, post-front layer is of order a few, so the speed of the I-front is lower than would be calculated using the unattenuated flux in the I-front continuity jump condition.

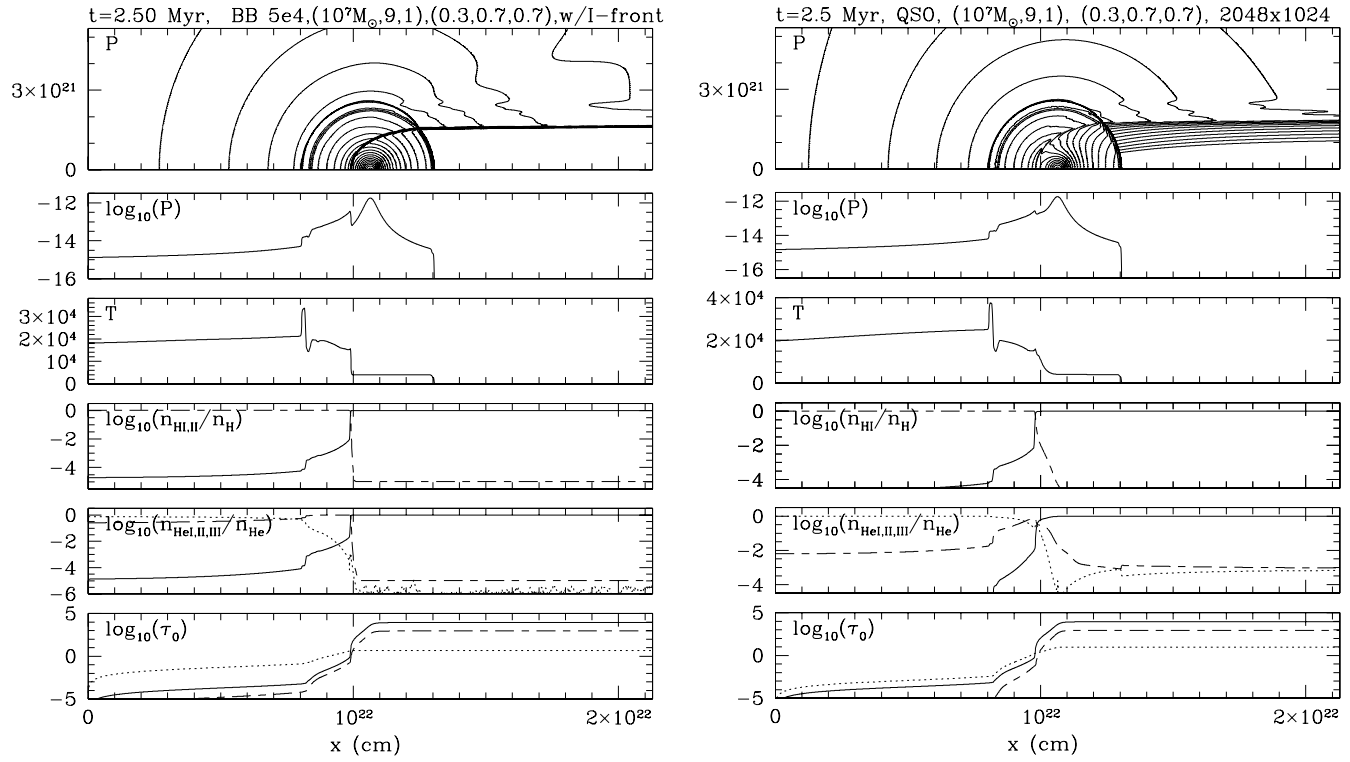

Figure 16. Weak, R-type phase of I-front inside the minihalo. Same as in Fig. 12, but for $t = 2.5$ Myr.

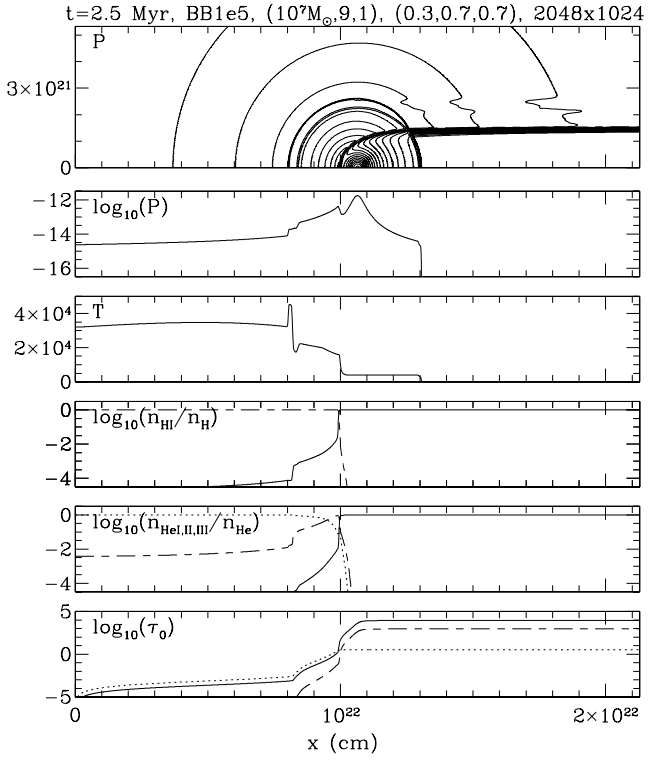

Figure 17. Same as in Fig. 16, but for the BB 1e5 case.

This R-critical phase is the beginning of the transition to D-type, which should occur shortly thereafter, when a shock wave forms to compress the gas ahead of the front, to enable the front velocity to drop to the D-critical value. In this case, using the sound speeds at 5 Myr reported above, the D-critical velocity is $v_{\rm D} \approx c^2_{\rm s,I,1}/(2c_{\rm s,I,2}) \cong 1.35$ km s$^{-1} \ll v_{\rm R}$. As we can see from the plot of $v_{\rm I}$ in Fig. 11, however, the transition from R-type to D-type is quite extended in time, lasting tens of Myr. During that same time, the I-front advances into denser and denser neutral minihalo gas, which also slows the front quite apart from any dynamical compression which might lead the front. In the meantime, from the R-critical phase onward, the hydrodynamical response to the I-front becomes more and more dramatic.

5.4 The structure of the photoevaporative flow during the D-type I-front phase

When the I-front slows to become a D-type front, the hydrodynamical response of the gas catches up with it and leads to the complete photoevaporation of the minihalo. This photoevaporative flow exhibits many generic features which are independent of the spectrum of the ionizing source. The side facing the source expels a supersonic wind backwards towards the source. There is a wind shock which thermalizes this wind outflow and separates the unshocked supersonic wind close to the ionized side of the I-front from the shell of shocked wind further away from the I-front on this side. The shocked wind gas acts as a piston which sweeps up the photoionized IGM outside the minihalo and drives a shock into the IGM, reversing its infall velocity. The wind grows more isotropic with time as the remaining neutral halo material is photoevaporated. Since this gas was initially bound to a dark halo with $\sigma_V < 10$ km s^{-1}, photoevaporation proceeds unimpeded by gravity. In Figs 22–26, we show the structure of the flow at a time 60 Myr after the global I-front first overtakes the minihalo. In Fig. 22 and the left panels of Fig. 23 we show the density contours of the gas, the current position of the ionization front, the velocity field, the current extent of the original halo material, and profiles of gas number density, velocity and Mach

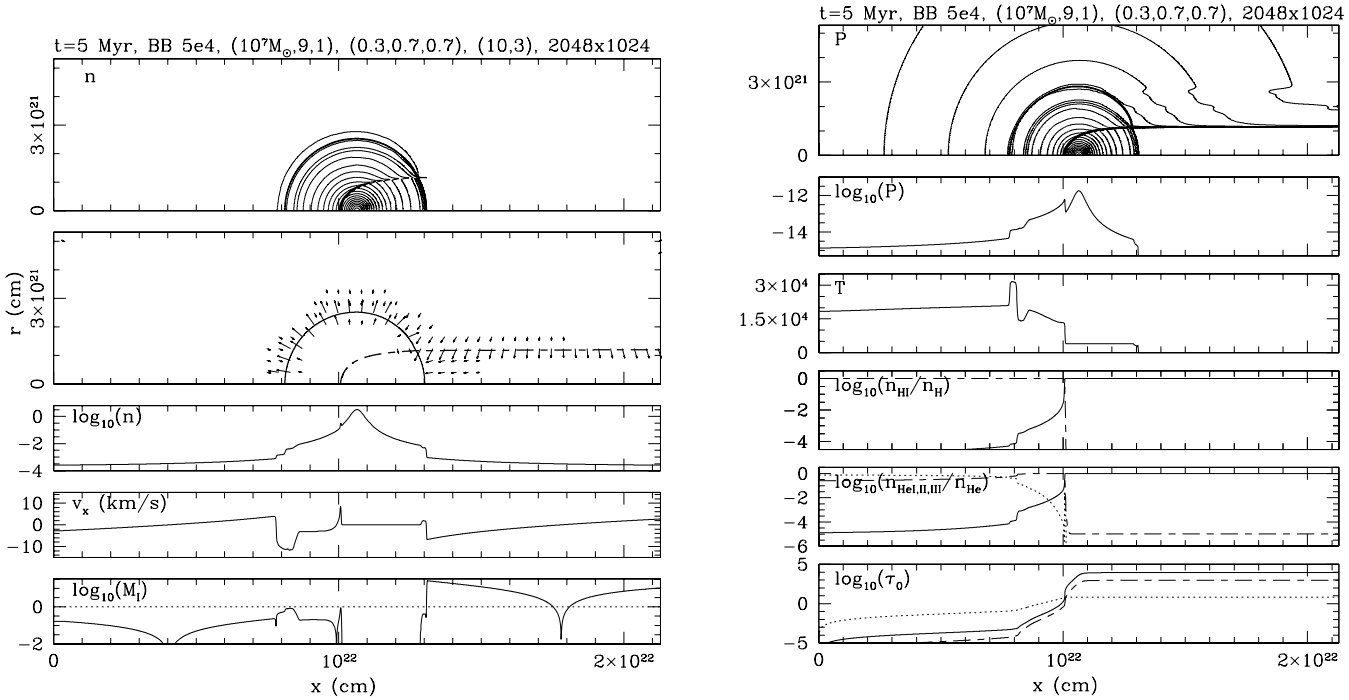

Figure 18. R-critical phase of the I-front just before transition from R-type to D-type. (a) (left) panels show the same quantities as in Fig. 14, but for the $t =$ 5 Myr and BB 5e4 case; (b) (right) same quantities as in Fig. 12, but for the $t = 5$ Myr and BB 5e4 case.

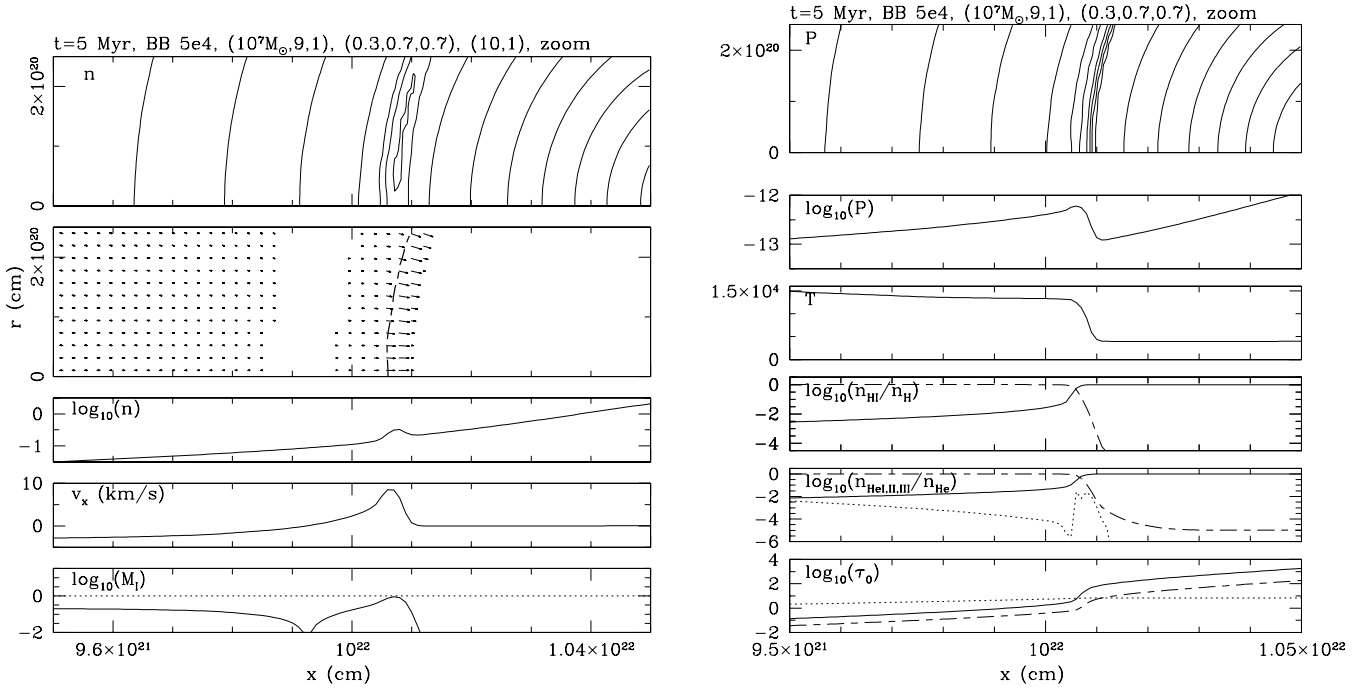

Figure 19. Same as in Fig. 18, but 'zoomed-in' to enlarge the view of the R-critical I-front along the *x*-axis.

number along the *x*-axis. In all three cases, the typical speed of the photoionized outflow is supersonic and roughly proportional to the sound speed of the ionized gas. Hence, the outflow is fastest in the BB 1e5 case, due to the higher photoionization temperature reached in this case.

For comparison, we have also performed a simulation of this problem in the optically thin approximation (i.e. zero optical depth), to demonstrate the inadequacy of such an approximation. In Fig. 23 (right panels), we plot the results for this optically thin photoevaporation simulation for exactly the same halo and source parameters as the BB 5e4 spectrum case shown in Fig. 22 (left panels), for the same time-slice. In the optically thin case, the halo is suddenly and uniformly ionized and photoheated to $T \sim 20\,000$–$35\,000$ K, well above its virial temperature. Thereafter, the large

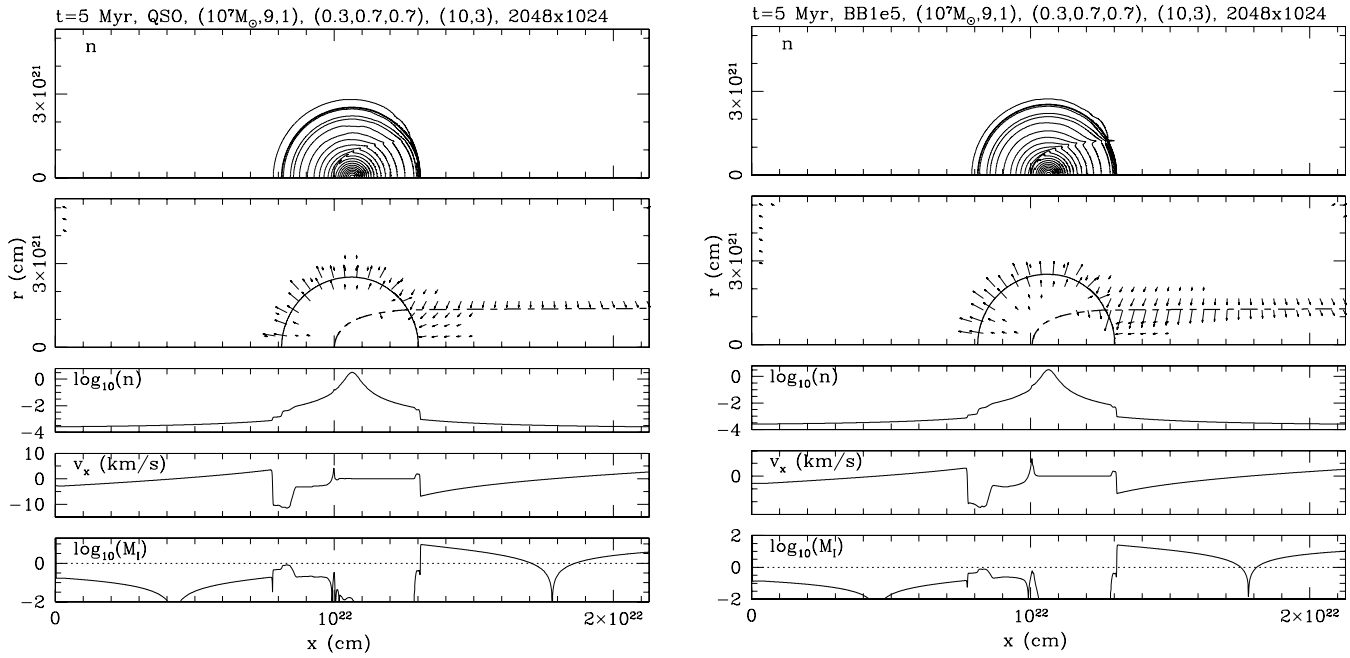

Figure 20. R-critical phase of the I-front just before transition from R-type to D-type. Panels show the same quantities as in Fig. 14, but for $t = 5$ Myr: (a) (left) QSO case; (b) BB 1e5 case.

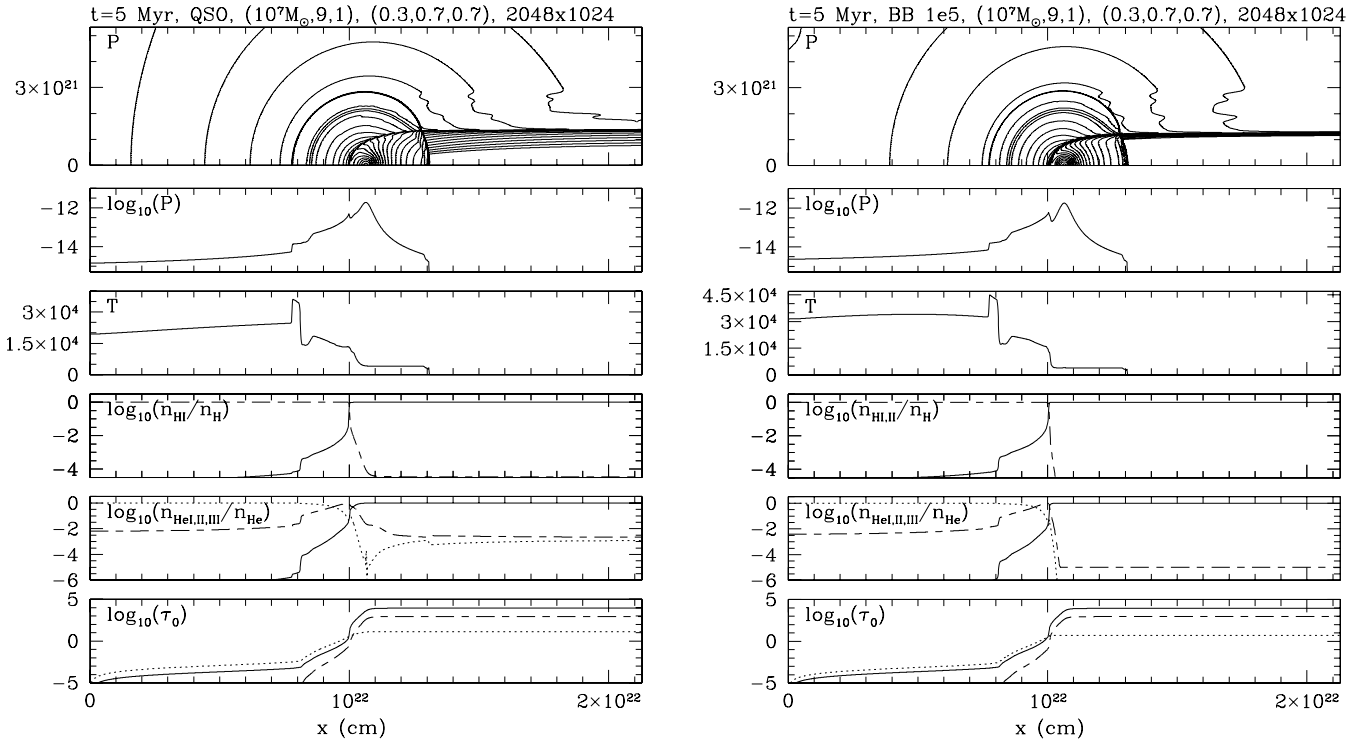

Figure 21. R-critical phase of the I-front just before transition from R-type to D-type. Panels show the same quantities as in Fig. 12, except for $t = 5$ Myr: (a) (left) QSO case; (b) BB 1e5 case.

pressure gradient causes the gas to expand isotropically in all directions unimpeded by gravity, producing a completely different flow structure.

For the more realistic simulations which included radiative transfer, Figs 24 and 25 show the pressure contours, and the profiles along the symmetry axis for pressure, temperature, H I–II fractions, He I–III fractions, and optical depths at the ionization thresholds of H I, He I, and He II, for the photoevaporative flow 60 Myr after the global I-front first overtakes the minihalo. Key features of the flow are indicated by the labels on the temperature panels. For comparison, we also show the very different results for these quantities in the optically thin simulations (Fig. 25, right panels).

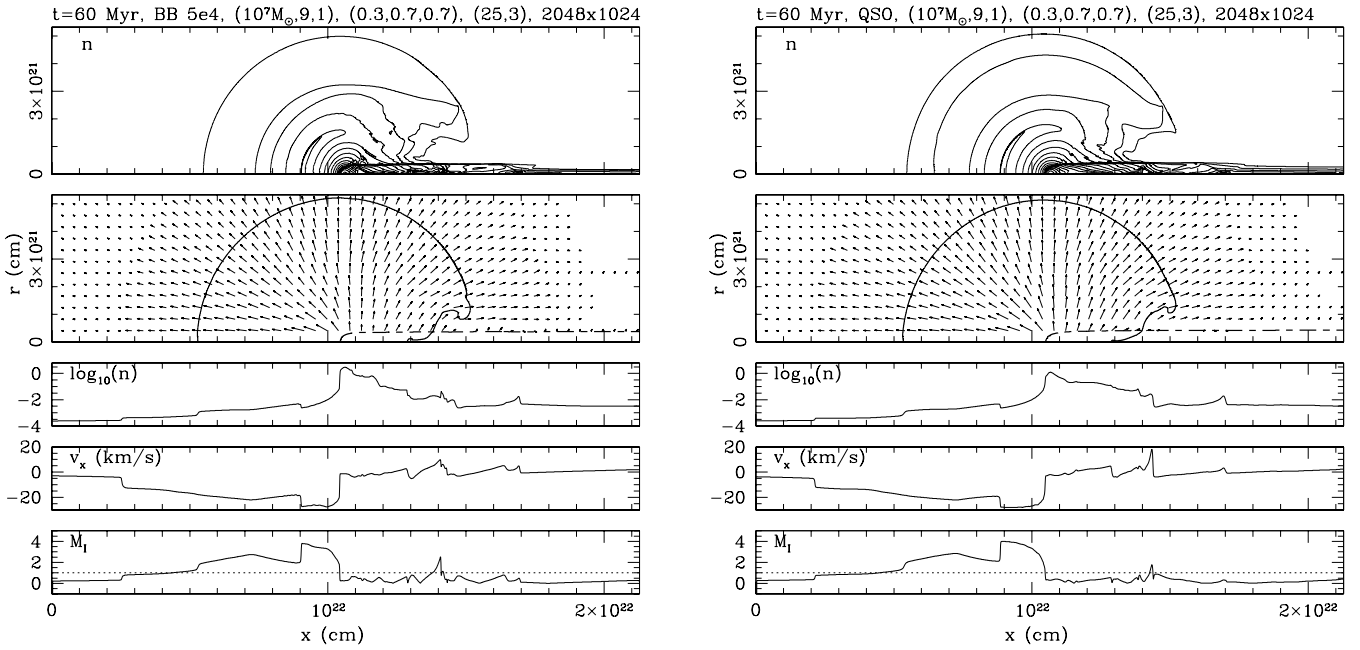

Figure 22. D-type phase of the I-front: photoevaporative flow 60 Myr after the I-front overtakes the minihalo: (a) (left) BB 5e4 case and (b) (right) QSO case. Same quantities plotted as in Fig. 14, except $t = 60$ Myr.

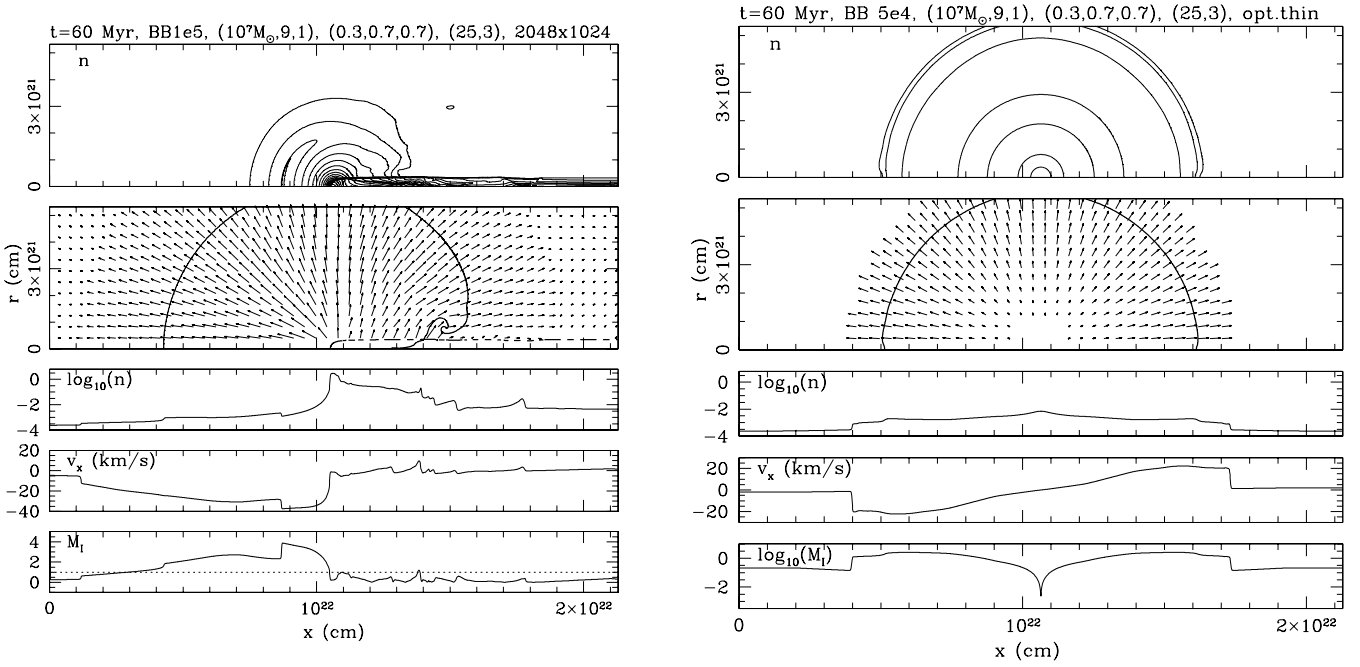

Figure 23. (a) (Left) same as Fig. 22, but for the BB 1e5 case. (b) (Right) same time-slice as Fig. 22, but for the optically thin BB 5e4 case.

5.5 Evolution of the temperature structure

The different stages of the photoevaporation process are illustrated in Fig. 26 by shaded isocontours of temperature for a sequence of time-slices of the BB 5e4 case. The panels show: (top left) (time $t = 0$ Myr), the initial condition of the isothermal, virialized halo surrounded by a cold, infalling, IGM; (top right) ($t = 0.2$ Myr), the fast, R-type I-front sweeping through the computational box is just about to encounter the minihalo along the x-axis, and is starting to photoheat the halo on the source side; (middle left) ($t = 2.5$ Myr), when the weak, R-type I-front is inside the minihalo before it slows to R-critical and begins to transform to D-type, a distinct shadow is apparent behind the neutral portion of the halo, while the rest of the gas is heated to $T > 10^4$ K, and the photoevaporation process begins; (middle right) ($t = 10$ Myr), the R-type to D-type transition phase, when the I-front slowly advances along the axis, the shadow region behind the shielded, neutral minihalo core is reduced, and the IGM shock and the shocked wind are clearly visible; (bottom left) ($t = 60$ Myr), strong D-type phase, when the shadow is being ablated and the remaining gas

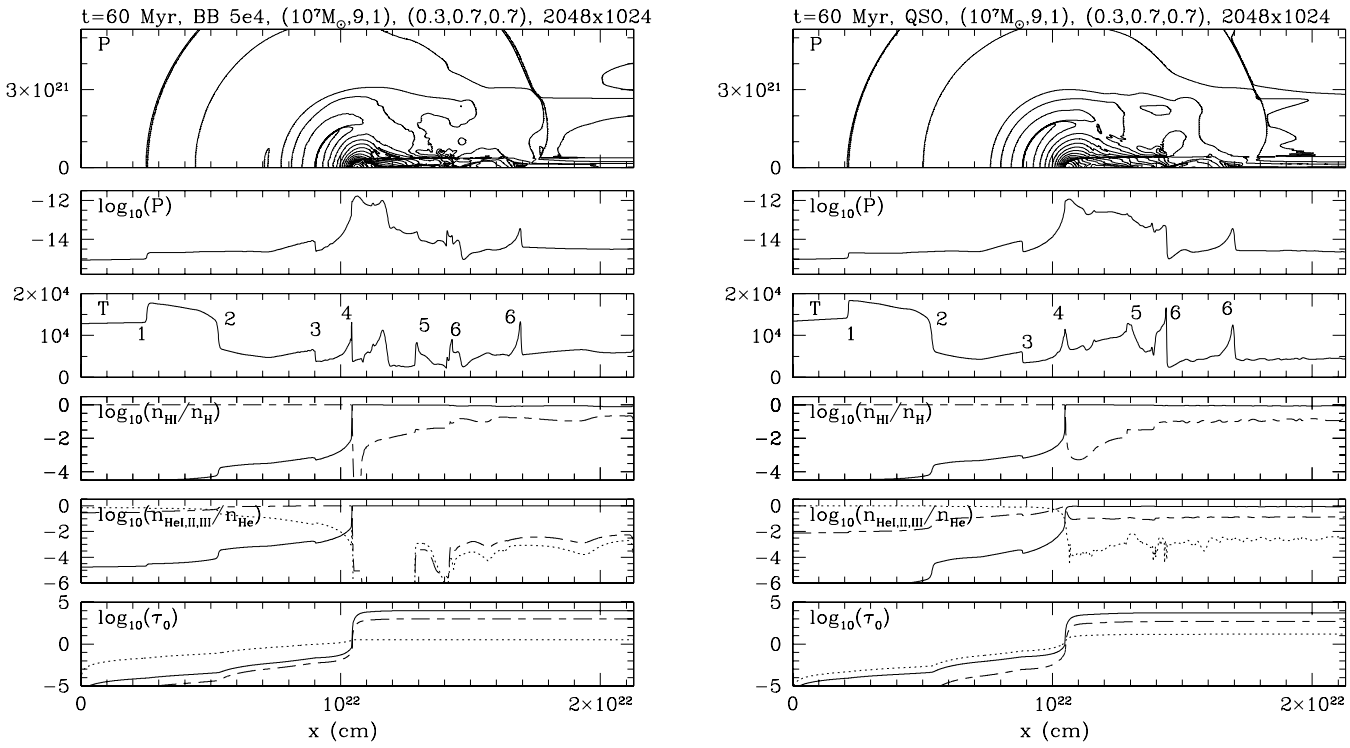

Figure 24. D-type phase of I-front: photoevaporative flow 60 Myr after the I-front overtakes the minihalo: (a) (left) BB 5e4 case and (b) (right) QSO case. Panels show the same quantities as in Fig. 12. Key features of the flow are indicated by the numbers which label them on the temperature plots: 1 = IGM shock; 2 = contact discontinuity which separates the shocked halo wind (between 2 and 3) from the swept-up IGM (between 1 and 2); 3 = wind shock; between 3 and 4 = supersonic wind; 4 = I-front; 5 = boundary of gas initially inside minihalo at $z = 9$; 6 = shock in shadow region caused by compression of shadow gas by shock-heated gas outside the shadow.

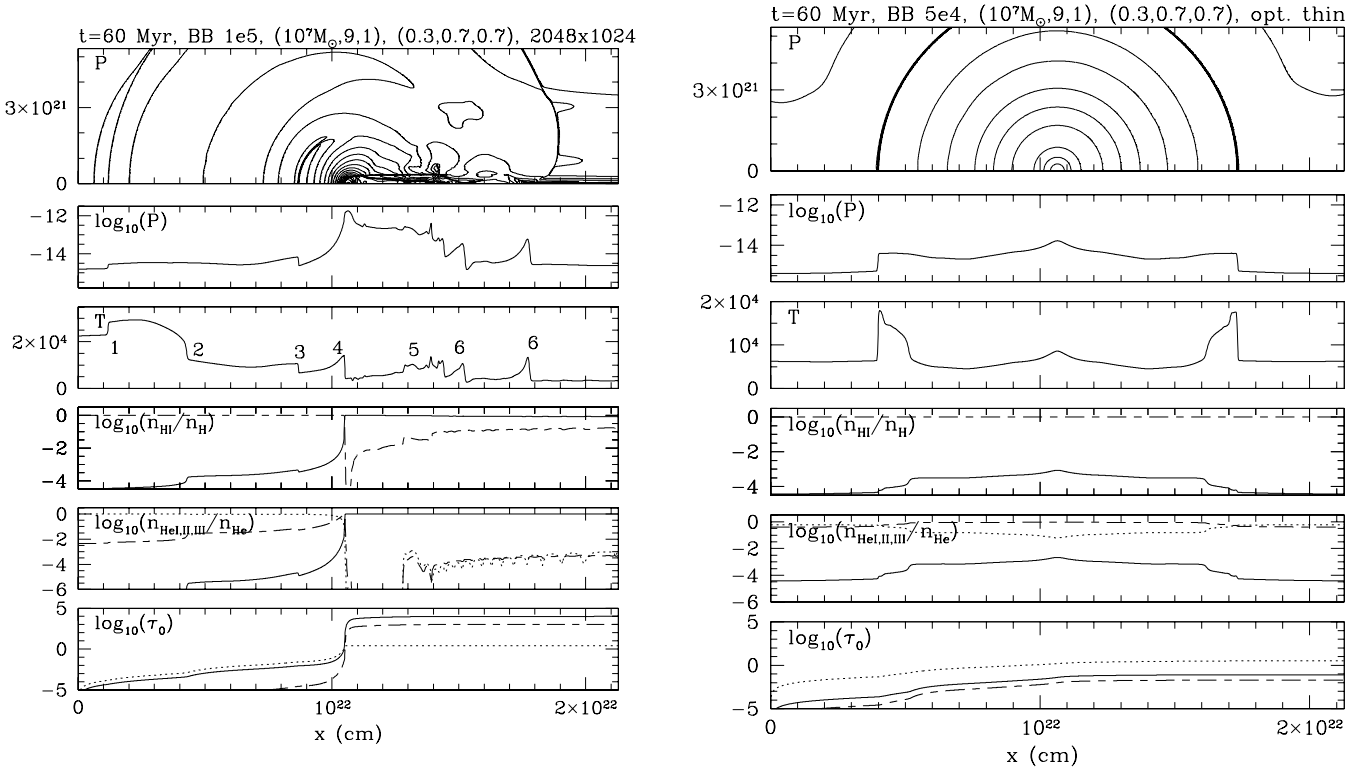

Figure 25. (a) (Left) same as Fig. 24, but for the BB 1e5 case. (b) (Right) same as Fig. 24, but for the optically thin BB 5e4 case.

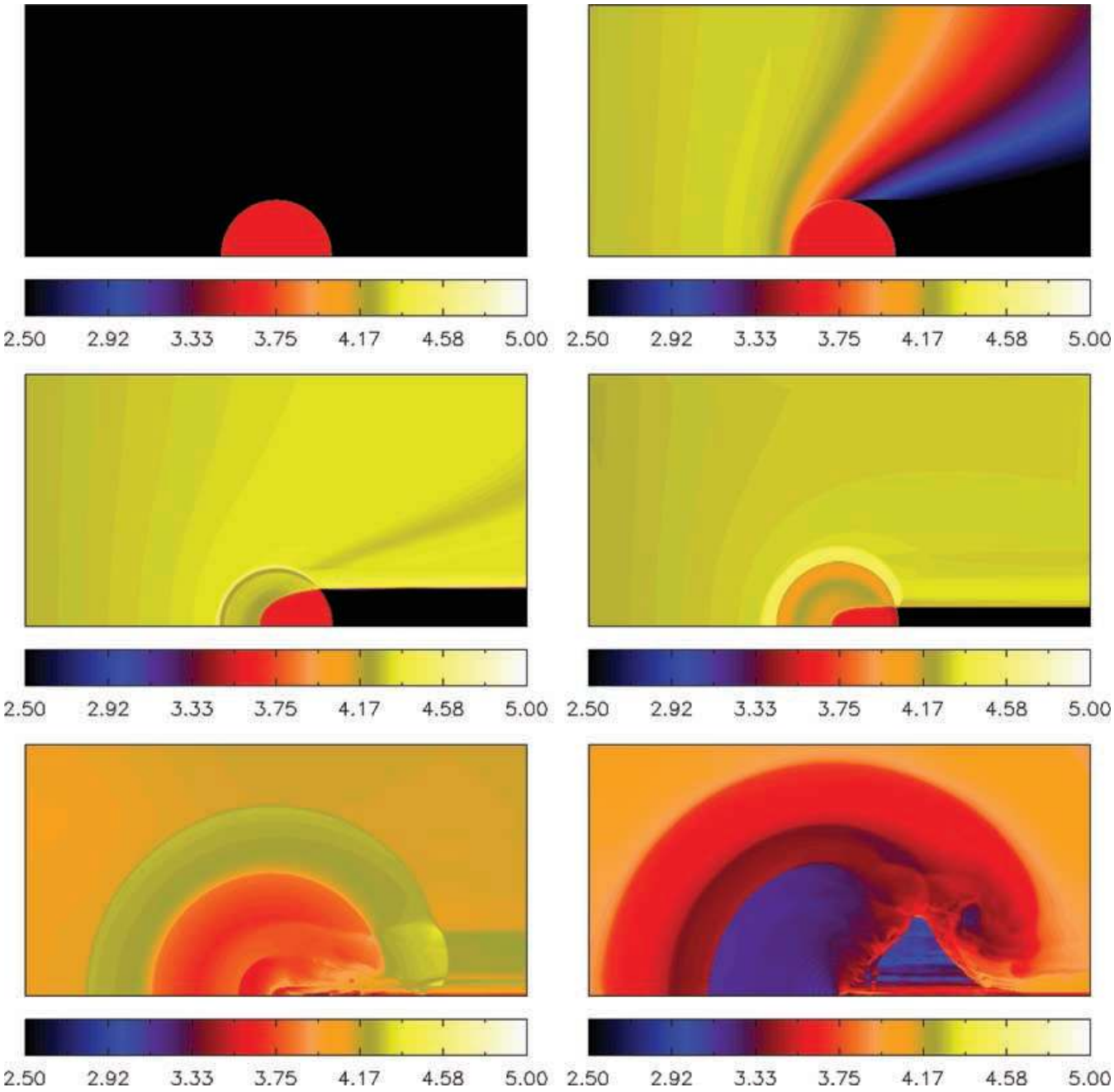

Figure 26. Snapshots of the temperature at times $t = 0$ (top left), 0.2 (top right), 2.5 (middle left), 10 (middle right), 60 (bottom left) and 150 (bottom right) Myr in the BB 5e4 case. Shaded isocontours are logarithmic in temperature. Colours indicate the values of $\log_{10}(T)$, as labelled on the colour bar.

heated, by weak shocks reflected off the x-axis behind the halo. The key features of the flow indicated in Fig. 24 are all clearly seen; (bottom right) ($t = t_{\rm ev} = 150$ Myr, the evaporation time), when the gas is almost completely evaporated from the halo and resides in a much larger, low-density region which is cooling adiabatically as it expands, leaving behind a dark-matter halo almost completely devoid of gas. The blue triangle in Fig. 26, bottom right panel is a region of very low density which was cooled by adiabatic expansion. This low-density region results when the remaining neutral gas shown in the bottom left panel is squeezed towards the axis of symmetry by the higher pressure of the expanding shells of shocked, ionized gas in the evaporative wind and swept-up IGM which surround it, causing a sequence of compressions and rarefactions to approach and reflect off the axis. Each reflection lifts another layer of shadowed neutral gas out of the shadow, which exposes it to the unattenuated ionizing flux, photoionizing and heating this gas, thereby increasing its pressure and causing it to expand. This makes more compressions and rarefactions reflect off the axis, ablating the remaining gas in the shadow region, layer by layer. The expanding shells of shocked gas in the evaporative wind and swept-up IGM outside the blue triangle add to the complexity of this phase of the flow, by converging on the x-axis beyond the minihalo, which causes vortical motion to occur behind these expanding shells. Movies of these simulation results, including the time evolution of additional quantities like density, and the H I and He I and C IV fractions, and results for cases with different source spectra are available at http://galileo.as.utexas.edu.

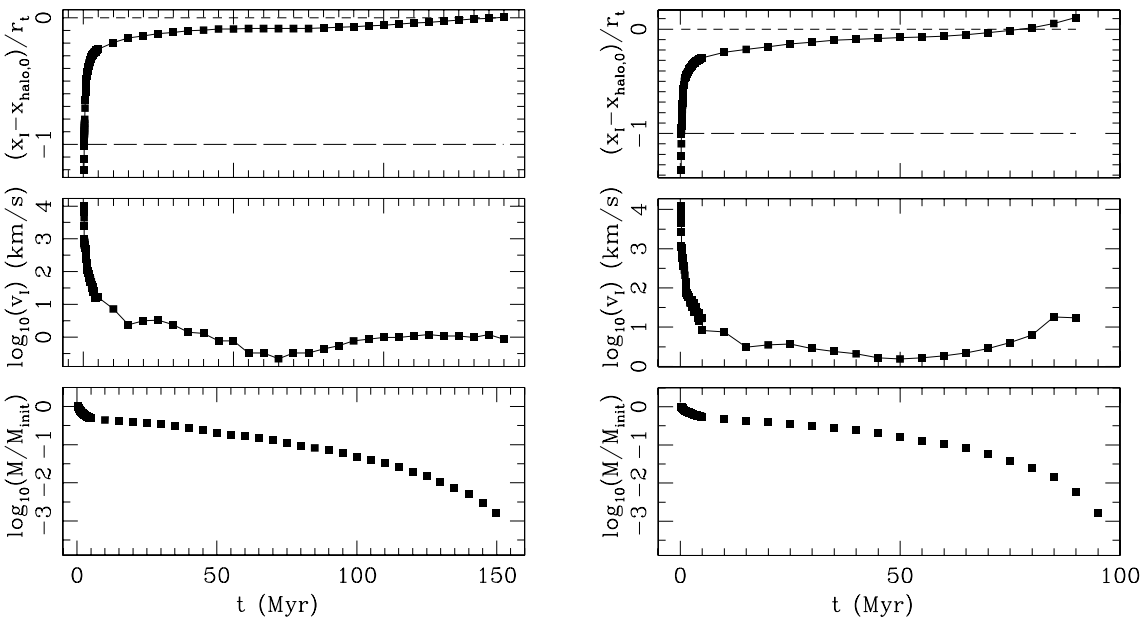

Figure 27. Evolution of I-front position and velocity and of the neutral gas content of a photoevaporating minihalo: (a) (left) BB 5e4 case and (b) (right) QSO case. (Upper panels) position x_I (in units of the minihalo radius r_t at $t = 0$) and (middle panels) velocity v_I of an ionization front propagating toward and through the minihalo. The positions of the boundary (long-dashed line) and centre of the halo (short-dashed line) are also indicated. (Lower panels) fraction of mass M_{init}, the mass which is initially inside the minihalo when the intergalactic I-front overtakes it, which remains neutral versus time t.

5.6 I-front evolution

The evolution of the position x_I and velocity v_I of the I-front, and of the remaining neutral mass fraction M/M_{init} are shown for all three source spectra cases in Figs 27 and 28, for comparison. The weak, R-type I-front slows down to the R-critical velocity about 5 Myr after it reaches the minihalo, after which a shock must form ahead of the I-front to compress the gas and slow it down to D-critical velocity or below, as discussed in detail in Section 5.2. The further evolution is slower and more gradual. Eventually, the I-front speed drops below the D-critical front speed $v_D \approx 1$ km s^{-1}. For the rest of the evaporation process, the velocity of the I-front is $\lesssim 1$ km s^{-1}, i.e. subcritical. At 60 Myr, for example, the I-front velocity has dropped to about $v_I \sim 0.3$ km s^{-1}, while the D-critical velocity is still $v_I \approx 1$ km s^{-1}. This behaviour is different from the usual approximation made in analytical calculations of photoevaporation, in which the I-front is assumed to be D-critical.

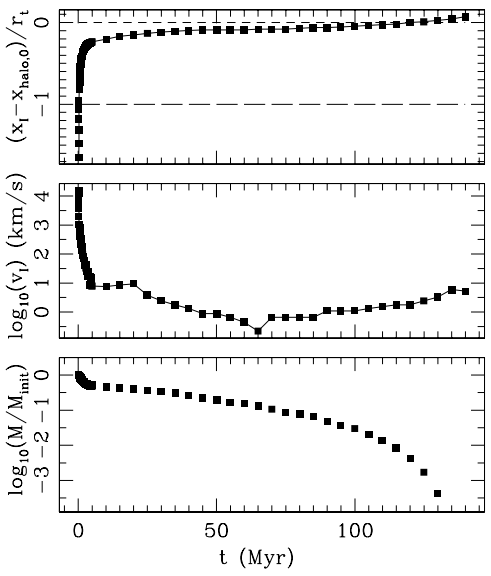

Figure 28. Same as in Fig. 27, but for the BB 1e5 case.

What kind of D-type front is it during the D-type phase? Weak, D-type fronts move subsonically with respect to both the neutral and ionized gas. Strong D-type fronts move subsonically into the neutral gas but supersonically with respect to the ionized gas. In the laboratory frame (i.e. the rest frame of the neutral gas before ionization), as the D-type front advances into the neutral side (i.e. away from the source), the ionized gas behind it always moves *toward* the source (i.e. opposite to the direction of the I-front). This ionized gas motion can be either subsonic (for weak fronts), or almost sonic (for D-critical fronts), but it is supersonic only for *strong* D-type fronts. If we apply this description to our 60-Myr time-slice for the BB 5e4 case and look both at the I-front velocity evolution plot in Fig. 27 and the cuts along the x-axis in Fig. 22, we see that the I-front is subcritical at that point. From the Mach number plot at points just behind the I-front on the immediate post-front (ionized) side, the laboratory frame velocity is supersonic toward the source, which indicates that the front is a strong, D-type. This is consistent with the density cut along the x-axis which shows that density *drops* by a very large amount from the neutral to the ionized side, as it should for both weak and strong, D-type fronts, but the strong type has an even bigger drop in density, as required to explain the numerical results. In short, the I-front at 60 Myr is a subcritical, strong, D-type.

5.7 Evaporation times

The neutral mass fraction of the original minihalo gas quickly drops to ∼60 per cent during the initial slowing-down phase of the I-front evolution, and subsequently declines much more gradually as the minihalo photoevaporates. We define the photoevaporation

time t_{ev} as the time when only 0.1 per cent of the mass remains neutral (i.e. when $M/M_{init} = 10^{-3}$). We see from Figs 27 and 28 that, once the neutral mass fraction reaches ~ 1 per cent, it drops fairly precipitously, indicating that the value of t_{ev} is not sensitive to our particular choice of the final value for M/M_{init} used to define this evaporation time. We obtain $t_{ev} \approx 150$, 125 and 100 Myr for the BB 5e4, BB 1e5 and QSO cases, respectively. Compared to the BB 5e4 case, the evaporation time in the BB 1e5 case is shorter due to the higher outflow velocity in this case (see Fig. 23), caused by the higher temperature in the photoionized region. In the QSO case, on the other hand, the outflow velocity is similar to the one in the BB 5e4 case, but the photoevaporation process in this case is accelerated by the significant pre-heating due to the hard photons present in this spectrum, which ultimately leads to an even shorter t_{ev}. These values of t_{ev} are all within a factor of 2 of the sound crossing time for an ionized gas sphere of the same diameter as our minihalo reported in Section 2.4. However, we caution that this result is not a proof that t_{sc} is a good estimator of t_{ev}. In fact, results for a wide range of halo and source parameters which we shall present in a companion paper demonstrate that t_{ev} departs significantly from t_{sc}, in general.

5.8 Ionizing photon consumption

5.8.1 Minihalo effective cross-section

The gradual decay of the opaque cross-section of the minihalo as seen by the source (as defined in equation 27) is illustrated by Fig. 29 (left panels) for photons at the ionization thresholds of H I, He I and He II. For the BB 5e4 case, the cross-section at the H I threshold drops to 10 per cent of its original value after $0.4t_{ev} = 60$ Myr, while the cross-section at the He I threshold drops somewhat faster. The cross-section of the minihalo at the He II threshold, however, initially rises as the partially ionized gas expands, and only later, around $0.4t_{ev} = 60$ Myr, does it start to decline slowly, as He II starts to become ionized to He III. The evolution of the H I effective cross-section is similar for the two stellar spectra, but decreases somewhat more slowly in the QSO case, while the evolution of the He I cross-section is similar for all three spectra. Finally, the evolution of the He II cross-section is markedly different in all three cases, due to the different photon energy distributions of the three spectra.

In Fig. 29, we show the transmitted fluxes at the ionization thresholds of H I, He I and He II versus impact parameter r at times $t =$ 5, 25, 50, 100 and 150 Myr for the BB 5e4 case. We see that the simulation box is optically thin to the photons with energies below the He II ionization threshold along most lines of sight along the x-direction outside the minihalo; only the minihalo is significantly opaque, once the global I-front has swept past the minihalo. The cross-section of the minihalo declines quickly with time once the I-front enters it and is somewhat smaller for He I ionizing photons than for H I ionizing photons. The simulation box is never completely optically thin to He II ionizing photons and has rather complex time behaviour as the wind expands and more He II is photoionized to He III.

5.8.2 Number of ionizing photons per atom consumed during photoevaporation

Based on our simulation data, we have calculated the number of ionizing photons per atom, ξ, required to evaporate a minihalo both by using the effective cross-section method of equation (29) and by counting the total number of recombinations (as in equation 30). Using the first method, we obtain $\xi = (4.51, 5.41, 3.43)$ in the BB 5e4, QSO, and BB 1e5 cases, respectively, while the second method yields $\xi = (5.1, 5.0, 3.3)$. Since the two methods give similar results, we can, henceforth, rely upon either one. For the 'efficiency' factor

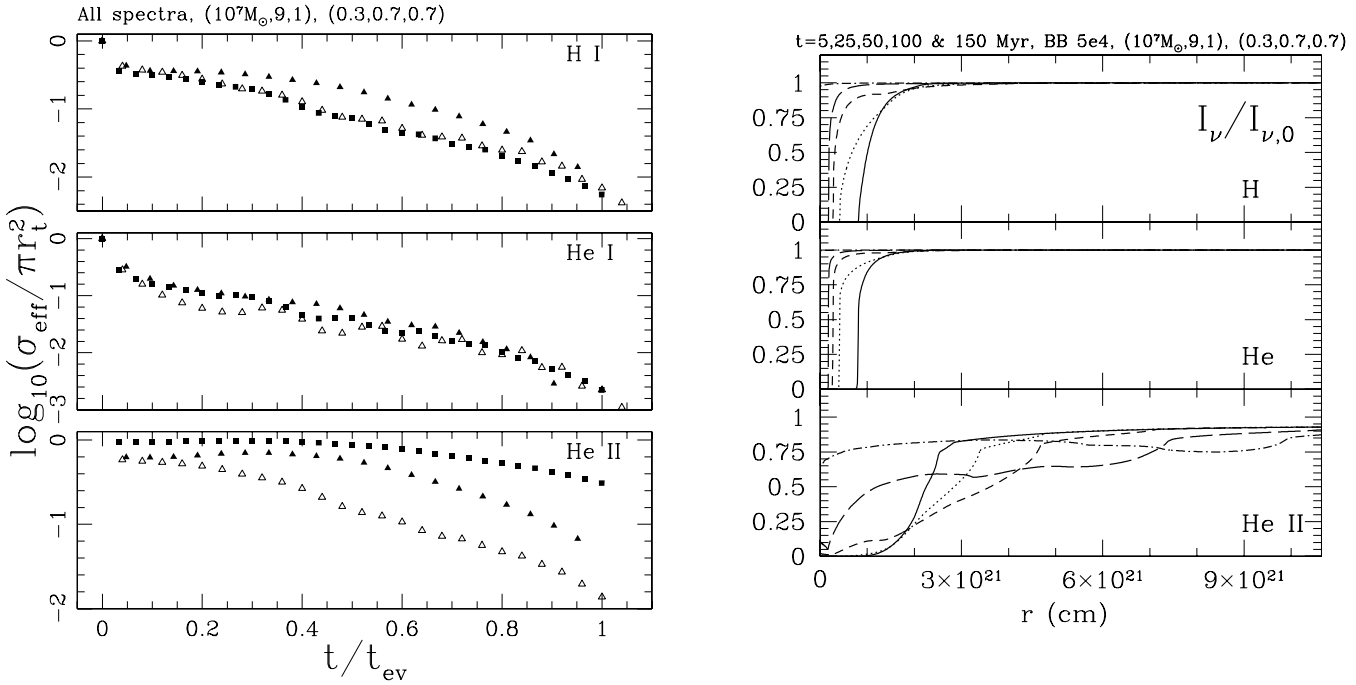

Figure 29. (a) (left) fraction of minihalo initial geometric cross-section πr_t^2 ($r_t = 0.76$ kpc) which is opaque to source photons that can ionize H I (top panel), He I (middle panel) or He II (bottom panel) versus time (in units of t_{ev}), for the BB 5e4 (filled squares), QSO (filled triangles) and BB 1e5 (open triangles) cases ($t_{ev} = 150$, 100 and 125 Myr, respectively). (b) (right) transmitted flux $I_\nu/I_{\nu,0}$ at the ionization thresholds of H (top), He I (middle) and He II (bottom) versus impact parameter (or radius in axisymmetry) r at times $t = 5$ (solid), 25 (dotted), 50 (short-dash), 100 (long-dash), and 150 (dot-dash) Myr for the BB 5e4 case.

f in equation (32) (assuming $T_4 = 1$), these results imply $f = (0.029, 0.034, 0.022)$ and $f = (0.032, 0.032, 0.021)$, respectively.

In the optically thin approximation case, the effective cross-section is, by definition, zero at all times, and thus only the second method for calculation of ξ is applicable. By contrast with our results which took proper account of the optical depth in bound–free opacity, for which $f \approx 0.02$–0.03, our optically thin results for ξ ($\xi \approx 18$, case BB 5e4) yield $f \approx 0.1$ [inconsistent with the result $f \approx 1$ reported by Haiman et al. (2001)]. Hence, while the optically thin approximation significantly overestimates ξ, the OTS approximation of equation (32) with $f = 1$ used by previous authors is an order of magnitude higher still than that, completely inadequate for determining ξ.

The failure of the optically thin and OTS approximations is easily understood if we consider where and when most of the recombinations take place. In Fig. 30, we show the evolution of ξ for our illustrative simulations. During the initial R-type phase, the I-front deceleration phase, a significant fraction of the mass (∼40 per cent in our sample simulations) becomes ionized almost instantly, just as does the entire minihalo in the optically thin approximation. This gas is in the halo outskirts, however, where the density is low and where that density drops even further as the gas expands in the evaporative outflow, into the IGM, making recombination in this gas inefficient within 10–20 Myr. Most of the minihalo gas is initially shielded, however, and remains neutral for a much longer time. From this point on, the additional ionization of gas occurs only where the photoevaporation process is removing it by expelling it in a supersonic wind. For gas in the wind, the density becomes too low too soon for significant recombinations to occur there. Therefore, during most of the evolution, the bulk of the recombinations occur in a thin dense layer in the immediate vicinity of the I-front. Each gas atom spends only a short time in this layer, however, as it rushes supersonically away from the neutral region into the low-density expanding wind, hence experiencing many fewer recombinations than the optically thin approximation would have predicted.

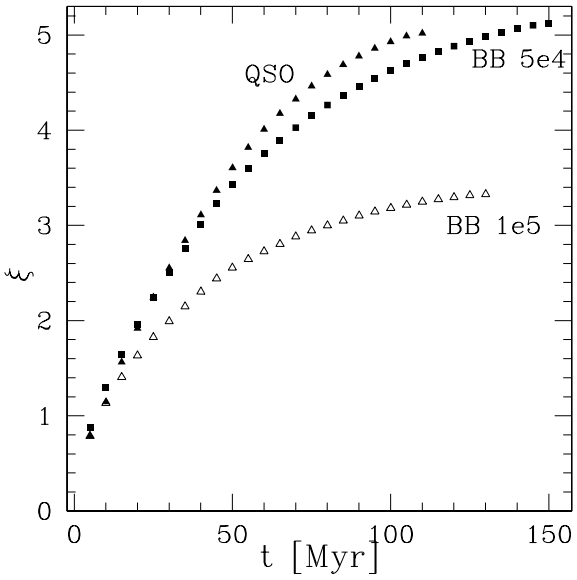

Figure 30. Evolution of the cumulative number of ionizing photons absorbed per initial minihalo atom, as given by equation (30) with $t_{\rm ev}$ replaced by t and with the first term on the right-hand side replaced by $N_{\rm ion}/N_{\rm a}$, where $N_{\rm ion}$ is the number of ionized minihalo atoms at time t, for all three spectra, as labelled.

As Fig. 30 shows, ξ increases gradually throughout the evaporation time, and there are noticeable differences among the three cases. For the hard QSO spectrum, the transition layer is thicker and penetrates deeper into the denser and colder parts of the halo, thus increasing the number of recombinations per atom per evaporation time. However, this same pre-heating effect shortens the evaporation time in this case, ultimately leading to a rough cancellation of the two effects and the same total ξ as in the BB 5e4 case. The BB 1e5 spectrum is not as hard as in the QSO case, which decreases the number of recombinations in the I-front layer. The evaporation time in this case is also shorter than in the BB 5e4 case, due to a higher photoionization temperature and thus to faster outflow speed. Additionally, the higher temperatures in the wind for the BB 1e5 case (∼10^4 K, as opposed to ∼5000 K in the other two cases, see Figs 24 and 25) also leads to lower rates of recombination in the wind and again lower ξ. Thus, overall, the Population III sources appear significantly more efficient than Population II or QSO sources in terms of the total number of ionizing photons needed to complete the photoevaporation process.

In principle, the optically thin approximation (but never the OTS approximation) might become correct in the limit of $\chi_{\rm S} \gg \chi_{\rm S,crit}$ (see Section 2.3), in which case the I-front is not trapped, the minihalo is ionized almost instantly compared to the evaporation time, and

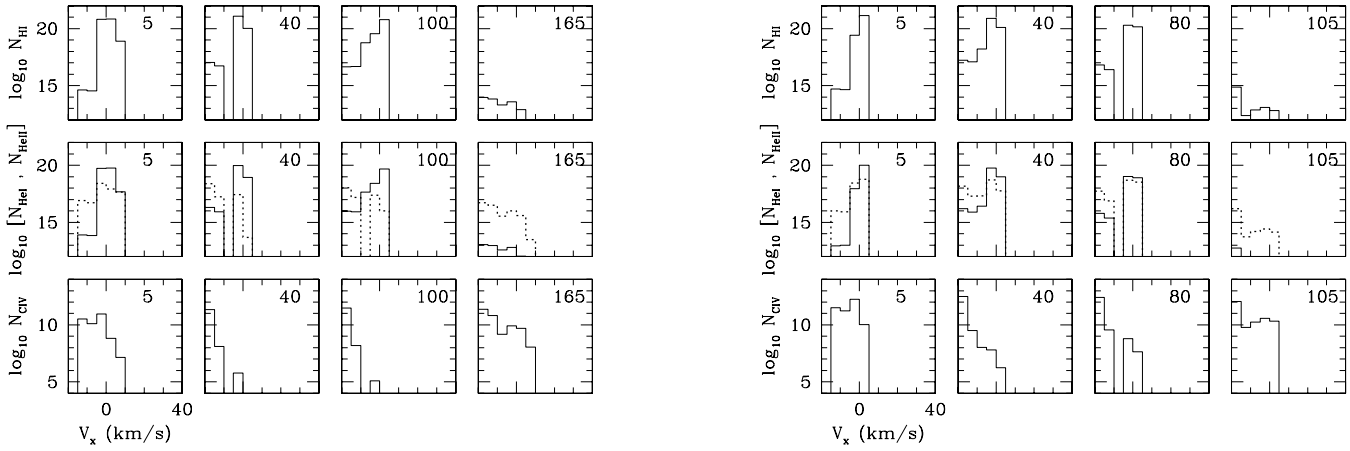

Figure 31. Observational diagnostics I: absorption lines. Minihalo column densities (cm^{-2}) along the symmetry axis for the gas at different velocities, for the photoevaporating minihalo. (a) (Left) BB 5e4 case; (b) (right) QSO case. (Top) H I; (middle) He I (solid) and He II (dotted); (bottom) C IV (if $[{\rm C}]/[{\rm C}]_\odot = \eta \times 10^{-3}$, then the plotted values are $N_{\rm CIV}/\eta$). Each box is labelled with time (in Myr) since the arrival of the intergalactic I-front.

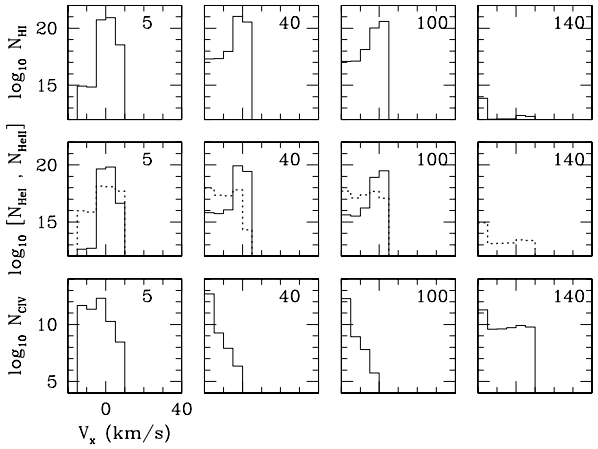

Figure 32. Same as in Fig. 31 but for the BB 1e5 case.

the radiative transfer effects are less significant. However, for most minihaloes this is not a relevant limit, since it requires an excessively high ionizing flux of $F_0 \gtrsim 100$–1000, depending on the halo mass and redshift of collapse (see Section 2.2).

5.9 Observational diagnostics

5.9.1 Absorption lines

Some observational signatures of the photoevaporation process are shown in Figs 31–34. In Figs 31 and 32, we show histograms of the column densities of H I, He I, He II and C IV for minihalo gas at different radial velocities as seen along the symmetry axis at different times, to illustrate the kind of absorption lines which a photoevaporating minihalo might produce. At early times, the minihalo gas resembles a weak damped Lyα (DLA) absorber with small velocity width ($\gtrsim 10$ km s^{-1}) and $N_{\rm HI} \gtrsim 10^{20}$ cm^{-2}, with a Lyα-forest (LF)-like red wing (velocity width $\gtrsim 10$ km s^{-1}) with $N_{\rm HI} \sim 10^{15}$ cm^{-2} on the side moving toward the source. As photoevaporation proceeds, this red wing increases in H I column density to $N_{\rm HI} \sim 10^{17}$ cm^{-2}. The He I profile mimics that of H I but with $N_{\rm He\,I}/N_{\rm HI} \sim$ [He]/[H], and there is a weak C IV feature with $N_{\rm CIV} \sim 10^{10}(10^{12})\eta$ cm^{-2} for the BB 5e4 (QSO, BB 1e5) cases, respectively, displaced in this same asymmetric way to the red side of the velocity of peak H I column density, where $\eta \equiv [\,{\rm C}]/[\,{\rm C}]_\odot \times 10^3$. For He II at early times, the QSO and BB 5e4 cases have $N_{\rm HeII} \approx 10^{18}$ cm^{-2} at velocities close to those of the H I peak, and a red wing shifted by $\sim$10 km s^{-1} to the red, with $N_{\rm HeII} \sim 10^{17}$ cm^{-2} which increases over time to 10^{18} cm^{-2}. He II qualitatively follows the H I and He I profiles in these cases. For the BB 1e5 case, however, $N_{\rm HeII} \approx 10^{18}$ cm^{-2} in the HI peak, at early times, decreasing to $N_{\rm HeII} \approx 10^{17}$ cm^{-2} over time, with a red wing with $N_{\rm HeII} \approx 10^{17}$ cm^{-2} which *increases* to $N_{\rm HeII} \approx 10^{18}$ cm^{-2}. In this case, the He II profile notably diverges from the H I profile. After about an evaporation time, both H I and He I column densities decrease to LF-like values of 10^{13}–10^{14} cm^{-2}, and shortly thereafter the minihalo is completely evaporated. Finally, the C IV column density is greatest in the red wing formed by the evaporative wind, except at the earliest times.

5.9.2 Ionization structure of metals

Figs 33 and 34 show the spatial variation of the relative abundances of C, N and O ions along the symmetry axis at $t = 60$ Myr. While the QSO case shows the presence at 60 Myr of low as well as high ionization stages of the metals, up to C V, N VI and O VI on the source side of the minihalo and C III on the neutral side, the softer spectrum of the BB 5e4 case yields less highly ionized gas both on the ionized side of the I-front (C III, N III, O III) and the neutral side (C II, N I, O I and O II). The BB 1e5 case is intermediate between the other two cases, ionizing carbon up to C V, but ionizing nitrogen and oxygen mostly to N IV and O IV, respectively, with smaller fractions of N V and O V and much smaller, although not negligible, fractions of N VI and O VI than in the QSO case. In the optically thin approximation case in Fig. 34 (right panels), similar

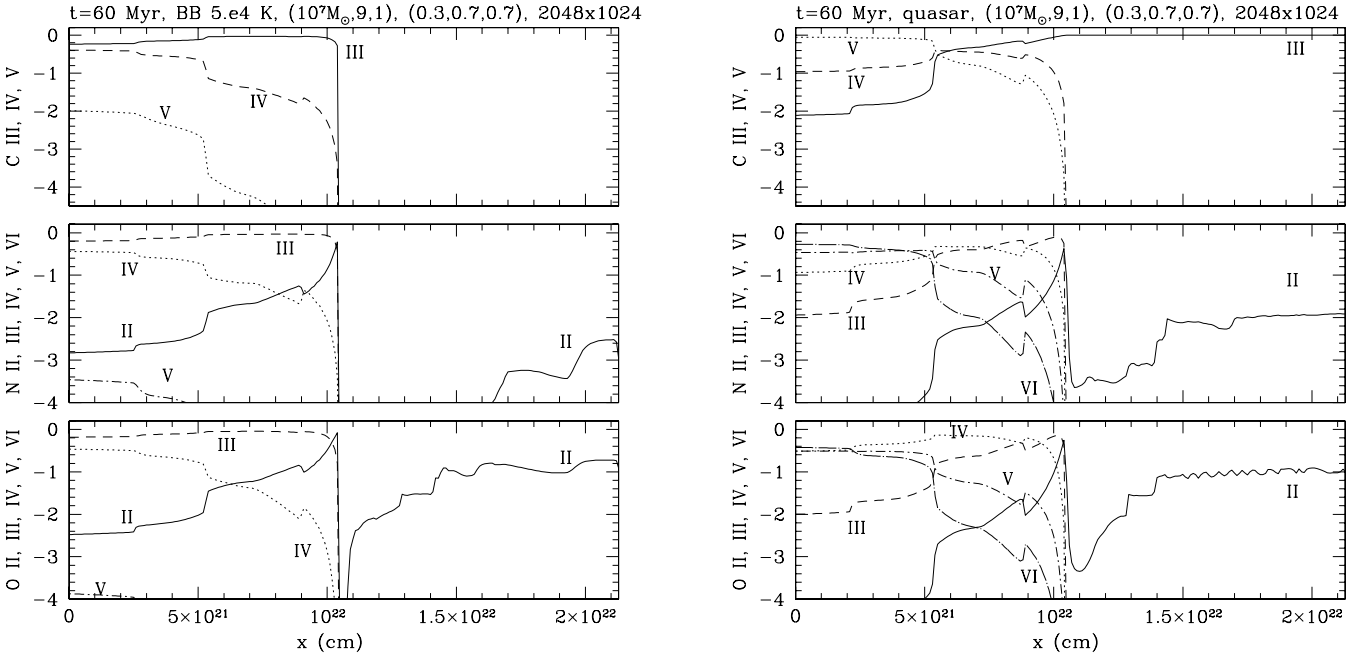

Figure 33. Observational diagnostics II: ionization structure of metals. C, N and O ionic fractions along the symmetry axis at $t = 60$ Myr, for the photoevaporating minihalo: (a) (left) BB 5e4 case; (b) (right) QSO case.

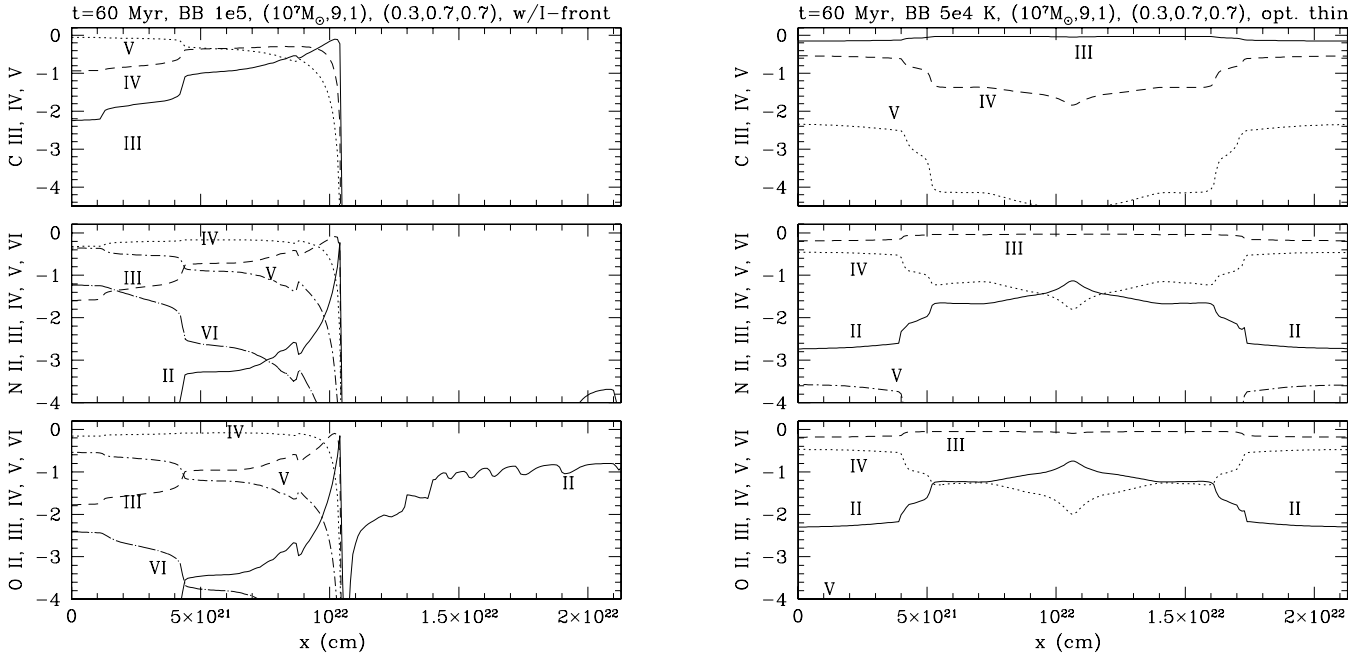

Figure 34. (a) (Left) same as Fig. 33, but for the BB 1e5 case. (b) (Right) same as Fig. 33, but for the optically thin BB 5e4 case.

high-ionization stages are reached for the ionized gas exposed to the same photoionizing spectrum as in the results above which took proper account of optical depth, but the low-ionization stages of neutral or partially ionized gas are entirely missing. In the optically thin results, all the gas is ionized instantly, no neutral region of minihalo or shadow exists and the flow expands symmetrically in all directions, which would lead to quite different spectral signatures as compared to the realistic optically thick cases shown above.

6 SUMMARY AND CONCLUSIONS

We have presented the first numerical gas dynamics and radiative transfer simulations of the encounter between an intergalactic I-front and a minihalo during cosmic reionization at high redshift, resulting in the photoevaporation of the minihalo gas. We have studied all stages of the photoevaporation process in detail, starting from the propagation of the fast, weak, R-type I-front in the low-density IGM, its structure and extent in pressure, temperature and ionization of H, He and a possible trace of metals for different possible source spectra, corresponding to quasars, Population III and Population II stars. We have demonstrated for the first time the phenomenon of I-front trapping when the global R-type I-front runs into a minihalo along its path and slows down inside the minihalo to an R-critical front, after which the front inside the minihalo transforms from an R-type to a D-type front. We have shown that the heated and ionized gas behind the front then expands supersonically into the IGM, sweeping it up and shock-heating it. This process exposes further layers of the minihalo gas to the ionizing radiation from the external source, heating and evaporating them until all the gas is finally expelled from the minihalo. For our illustrative case of a 10^7-$M_\odot$ halo, overtaken at $z = 9$ by an intergalactic I-front created by a source of 10^{56} ionizing photons per second at a distance of 1 Mpc (or equivalently, a source of 10^{52} s^{-1} at 10 kpc), this process is completed within ~100–150 Myr, depending on the source spectrum.

The results presented here are fully consistent with our earlier simulations of minihalo photoevaporation, going back to Shapiro et al. (1997, 1998) and continuing through those in Shapiro & Raga (2000a,b, 2001), and Shapiro (2001), although there are some quantitative differences which result from improvements we have made since then. However, these results differ from those which have appeared in the meantime in the recent literature. As mentioned in Section 1.3, for example, Barkana & Loeb (1999) considered the photoevaporation of minihaloes without gas dynamics and without treating the propagation of the I-front. Their calculations are similar in spirit to (albeit more sophisticated than) our analytical ISL approximation in Section 2.3. The result of their static approximation is that the larger minihaloes ($\geqslant$ few $\times$ 10^5–10^6 $M_\odot$, depending on the redshift and the source spectrum) were predicted not to evaporate completely but rather to leave a significant fraction of the gas (20–40 per cent for a QSO-type power-law spectrum for a 10^7-$M_\odot$ halo at $z = 8$–20) still gravitationally bound to the minihalo. Our illustrative simulations demonstrate that when dynamical evolution is included this is not the correct outcome and all the gas is evaporated from the minihaloes, leaving behind only a dark matter halo almost completely devoid of gas. In a companion paper, we will extend these studies to show that this conclusion holds for all minihaloes, independent of their mass and redshift of collapse.

We have also shown here that a hydrodynamical treatment of the photoevaporation of minihaloes which fails to include radiative transfer (i.e. the zero optical depth approximation) is also not adequate for describing this problem. Such an approximation yields a spherically symmetric outflow and uniformly high ionization structure which differ greatly from the more realistic results reported here which take radiative transfer into account. As a consequence, any observable features, such as absorption lines, would not be predicted correctly by this approximation. The difference between more realistic simulations like ours, which include radiative transfer, and those which neglect optical depth can have profound consequences for the theory of cosmic reionization, as well.

Haiman et al. (2001) pointed out the potential importance of minihaloes as sinks of ionizing photons during reionization, due to the increased recombination rate inside these high-density regions. In

Section 2.5, we described how these authors estimated, in the optically thin limit, the number of ionizing photons per atom ξ needed to evaporate a minihalo. They concluded from this that the clumping due to minihaloes can easily raise the number of photons required to complete reionization by an order of magnitude or more compared to estimates that ignored the minihaloes. This prompted them to identify a photon budget problem when comparing the requirements for reionizing the Universe with the available photon supply. In this paper, we have used our self-consistent gas dynamics and radiative transfer simulations to calculate ξ under more realistic assumptions. We have shown that the effect of ignoring radiative transfer and its feedback on the gas dynamics is to overestimate ξ significantly. For the illustrative cases shown here, we find that ξ was overestimated by a factor as large as 30–50, depending on the ionizing spectrum. In terms of the efficiency factor in equations (31) and (32), this means that we have found values of $f \sim 1/30$ to $1/50$, depending on the spectrum of the ionizing sources. Such optically thin estimates also do not account for differences due to differences in the external source spectra. We have shown that photoevaporation by Population III stars is significantly more efficient in terms of the net photon consumption by this process than is photoevaporation by QSO or Population II stellar sources, even when all sources emit the same number of H ionizing photons per unit time. These effects may help alleviate the photon budget problem posed by Haiman et al. (2001), especially if Population III sources dominated reionization.

Although we find here that ξ is smaller than previously estimated, the effects of minihaloes as screens and of their evaporation as a sink of ionizing photons during reionization may still be considerable. For one, we find $\xi \sim 5$, which is still large compared to unity. In addition, this value applies only to the particular illustrative case of a 10^7-$M_\odot$ minihalo exposed to a source with flux $F_0 = 1$ at $z = 9$. Only after we also calculate the values of ξ per minihalo for the full range of minihalo masses and redshifts and of source fluxes which can occur during reionization can we determine the full impact of the minihaloes on that process. We will report those results in a companion paper to follow. However, we can already see that, if the reionization epoch was extended in time, as described in Section 1.1, with the final overlap of isolated H II regions occurring at $z < 9$, then the neutral regions which were ionized during this late phase had a significant fraction ($\gtrsim$30 per cent) of their baryons collapsed into minihaloes. In that case, minihalo photoevaporation by the global I-fronts which reionized the Universe is likely to have dominated this final 'overlap' phase.

Apart from the destructive effects of intergalactic I-fronts on minihalo gas content described here, it has also been suggested that the same I-fronts might, instead, have a positive feedback effect on the minihaloes rather than photoevaporating them entirely. It has been proposed, for example, that under certain conditions, external ionizing radiation can cause the implosion of the minihalo gas, leading to the formation of globular clusters (Cen 2001). We have not observed such an effect in our simulations.

Finally, we note that intervening minihaloes are expected to be ubiquitous along the line of sight to high-redshift sources (Shapiro 2001). With photoevaporation times $t_{\rm ev} \gtrsim 100$ Myr, this process can continue down to redshifts significantly below $z = 10$. For stellar sources in the ΛCDM model, our simulations show that photoevaporation of a 10^7-$M_\odot$ minihalo which begins at $z_{\rm initial} = 9$ can take 150 Myr to finish, at $z_{\rm final} = 7.5$, during which time such minihaloes can survive without merging into larger haloes. Observations of the absorption spectra of high-redshift sources, such as QSOs, supernovae (SNe), starburst galaxies and GRB afterglows, perhaps including the very sources which reionized the Universe, should reveal the presence of these photoevaporative flows and provide a useful diagnostic of the reionization process.

As described in Section 1.1, the early start ($z \gtrsim 15$) and late finish ($z \sim 6$) for the reionization epoch implied by current observations are consistent with a picture in which the volume-filling factor of ionized patches of the Universe grew over time from $z \gtrsim 15$ until they finally overlapped at $z \sim 6$. In that case, the formation of minihaloes filled with neutral gas is likely to have proceeded inside the surviving neutral regions at the 'unfiltered' rate of the Universe without reionization. The I-fronts which led the expansion of the ionized patches would then have encountered fresh minihaloes of ever-increasing abundance over time, able to trap those I-fronts and be photoevaporated by them. Lines of sight through the neutral zones should, accordingly, encounter the greatest density of neutral-gas-filled minihaloes, while those through the ionized zones should sample photoevaporating minihaloes which trace the boundaries of the ionized patches. Inside these ionized zones, the abundance of minihaloes filled with neutral gas will drop over time, as photoevaporation proceeds to evacuate their gas as described here and as the reheated IGM resists further collapse into the new minihaloes which form there (e.g. Shapiro et al. 1994; Gnedin 2000b; Haiman et al. 2001; Cen 2003).

ACKNOWLEDGMENTS

We thank Garrelt Mellema for sharing his microphysics solver with us, for many useful discussions and for a careful reading of an early version of this manuscript. We thank Hugo Martel for discussion and collaboration on various aspects of the role of minihaloes which directly impacts the work reported here. We thank Marcelo Alvarez for his help in the visualization of our simulation results. This research was supported by NSF grant INT-0003682 from the International Research Fellowship Program and the Office of Multidisciplinary Activities of the Directorate for Mathematical and Physical Sciences, the Research and Training Network 'The Physics of the Intergalactic Medium' set up by the European Community under the contract HPRN-CT2000-00126 RG29185, NASA ATP Grant NAG5-10825, and Texas Advanced Research Program Grant 3658-0624-1999.

REFERENCES

Abel T. Norman M. L., Madau P., 1999, ApJ, 523, 66
Abel T. Bryan G. L., Norman M. L., 2002, Sci, 295, 93
Arthur S. J., 1991, PhD thesis, Univ. Leeds
Barkana R., Loeb A., 1999, ApJ, 523, 54
Barkana R., Loeb A., 2002, ApJ, 578, 1
Becker R. H. et al., 2001, AJ, 122, 2850
Bertoldi F., 1989, ApJ, 346, 735
Bertoldi F., Draine B., 1996, ApJ, 458, 222
Bertoldi F., McKee C. F., 1990, ApJ, 354, 529
Bertschinger E., 1985, ApJS, 58, 39
Binney J., Tremaine, S., 1987, Galactic Dynamics. Princeton Univ. Press, Princeton, NJ
Bond J. R., Szalay A. S., Silk J., 1988, ApJ, 324, 627
Bromm V., Kudritzki R. P., Loeb A., 2001, ApJ, 552, 464
Bromm V., Coppi P. S., Larson R. B., 2002, ApJ, 564, 23
Cen R., 2001, ApJ, 560, 592
Cen R., 2002, ApJS, 141, 211
Cen R., 2003, ApJ, 591, 12
Cen R., McDonald P., 2002, ApJ, 570, 457
Ciardi B., Ferrara A., Marri S., Raimondo G., 2001, MNRAS, 324, 381
Ciardi B., Stoehr F., White S. D. M., 2003, MNRAS, 343, 1101
Djorgovski S. G., Castro S., Stern D., Mahabal A. A., 2001, ApJ, 560, L5

Fan X. et al., 2000, AJ, 120, 1167
Fan X., Narayanan V. K., Strauss M. A., White R. L., Becker R. H., Pentericci L., Rix H.-W., 2002, AJ, 123, 1247
Fan X. et al., 2003, AJ, 125, 1649
Gnedin N. Y., 2000a, ApJ, 535, 530
Gnedin N. Y., 2000b, ApJ, 542, 535
Gnedin N. Y., Abel T., 2001, New Astron., 6, 437
Gorti U., Hollenbach D., 2002, ApJ, 573, 215
Haiman Z., Abel T., Rees M. J., 2000, ApJ, 534, 11
Haiman Z., Abel T., Madau P., 2001, ApJ, 551, 599
Hayes J. C., Norman M. L., 2003, ApJS, 147, 197
Hui L., Haiman Z., 2003, ApJ, 596, 9
Iliev I. T., Shapiro P. R., 2001, MNRAS, 325, 468
Iliev I. T., Shapiro P. R., 2003, in Bender R., Renzini A., eds, ESO Astrophys. Symp., The Mass of Galaxies at Low and High Redshift. Springer, Berlin, p. 160
Klein R. I., Sandford M. T., Whitaker R. W., 1983, ApJ, 271, L69
Kogut A. et al., 2003, ApJS, 148, 161
Lefloch B., Lazareff B., 1994, A&A, 289, 559
Leitherer C. et al., 1999, ApJS, 123, 3
Lizano S., Canto J., Garay G., Hollenbach D., 1996, ApJ, 468, 739
Machacek M. E., Bryan G. L., Abel T., 2001, ApJ, 548, 509
Machacek M. E., Bryan G. L., Abel T., 2003, MNRAS, 338, 273
Madau P., Rees M. J., 2000, ApJ, 542, L69
Mellema G., 1993, PhD thesis, Univ. Leiden
Mellema G., Raga A. C., Canto J., Lundquist P., Balick B., Steffen W., Noriega-Crespo A., 1998, A&A, 331, 335
Miralda-Escude J., Haehnelt M., Rees M. J., 2000, ApJ, 530, 1
Nakamoto T., Umemura M., Susa H., 2001, MNRAS, 321 593
Navarro J. F., Frenk C. S., White S. D. M., 1996, ApJ, 462, 563
Navarro J. F., Frenk C. S., White S. D. M., 1997, ApJ, 490, 493
Oh, P., Haiman, Z., 2003, MNRAS, 346, 456
Oort J. H., Spitzer L. R., 1955, ApJ, 121, 6
Raga A. C., Taylor S. D., Cabrit S., Biro S., 1995, A&A, 296, 833
Raga A. C., Mellema G., Lundquist P., 1997, ApJS, 109, 517
Razoumov A. O., Scott D., 1999, MNRAS, 309, 287
Ricotti M., Gnedin N. Y., Shull J. M., 2001, ApJ, 560, 580
Ricotti M., Gnedin N. Y., Shull J. M., 2002a, ApJ, 575, 33
Ricotti M., Gnedin N. Y., Shull J. M., 2002b, ApJ, 575, 49
Sandford M. T., Whitaker R. W., Klein R. I., 1983, ApJ, 260, 183
Schmidt-Voigt M., Koeppen J., 1987, A&A, 174, 211
Shapiro P. R., 1986, PASP, 98, 1014
Shapiro P. R., 2001, in Wheeler J. C., Martel H., eds, AIP Conf. Proc. Vol. 586, Relativistic Astrophysics: 20th Texas Symp. Am. Inst. Phys., Woodbury, NY, p. 219
Shapiro P. R., Giroux M. L., 1987, ApJ, 321, L107
Shapiro P. R., Kang H., 1987, ApJ, 318, 32
Shapiro P. R., Raga A. C., 2000a, in Arthur S. J., Brickhouse N., Franco J. J., eds, Rev. Mex. Astron. Astrophys. Conf. Ser. Vol. 9, Astrophysical Plasmas: Codes, Models, and Observations. Inst. Astronomia, México, p. 292
Shapiro P. R., Raga A. C., 2000b, in Franco J., Terlevich E., Lopez-Cruz O., Aretxaga I., eds, ASP Conf. Ser. Vol. 215, Cosmic Evolution and Galaxy Formation: Structure, Interactions, and Feedback. Astron. Soc. Pac., San Francisco, p. 1
Shapiro P. R., Raga A. C., 2001, in Lee W., Torres-Peimbert S., eds, Rev. Mex. Astron. Astrophys. Conf. Ser. Vol. 10, The Seventh Texas-Mexico Conference on Astrophysics: Flows, Blows, and Glows. Inst. Astronomia, México, p. 109
Shapiro P. R., Giroux M. L., Babul A., 1994, ApJ, 427, 25
Shapiro P. R., Raga A. C., Mellema G., 1997, in Petitjean P., Charlot S., eds, Proc. 13th IAP Astrophys. Colloq., Structure and Evolution of the Intergalactic Medium from QSO Absorption Line Systems. Inst. Astrophys. Paris, Paris, p. 41
Shapiro P. R., Raga A. C., Mellema G., 1998, Mem. Soc. Astron. Ital., 69, 463
Shapiro P. R., Iliev I. T., Raga, A. C., 1999, MNRAS, 307, 203
Shapiro P. R., Iliev I. T., Raga, A. C., Martel H., 2003, in Holt S., Reynolds C., eds, AIP Conf. Ser., The Emergence of Cosmic Structures. Am. Inst. Phys., Woodbury, NY, p. 89
Sokasian A., Abel T., Hernquist L. E., 2001, New Astron., 6, 359
Spergel, D. et al., 2003, ApJS, 148, 175
Spitzer L. R., 1978, Diffuse Matter in Space. Wiley, New York
Tan J. C., McKee C. F., 2001, in Tacconi L., Lutz D., eds, Starburst Galaxies: Near and Far. Springer-Verlag, Heidelberg, 188
Tenorio-Tagle G., Bodenheimer P., Noriega-Crespo A., 1983, in Pequignot D., ed., Workshop on model nebulae. Observatoire de Paris, Paris, 178
Tumlinson J., Shull J. M., 2000, ApJ, 528, L65
van Leer B., 1982, Lect. Notes Phys., 170, 507
Venkatesan A., Giroux M. L., Shull J. M., 2001, ApJ, 563, 1
Yoshida, N., Abel T., Hernquist L., Sugiyama N., 2003, ApJ, 592, 645

APPENDIX A: A TIME-DEPENDENT MODEL FOR VIRIALIZED HALOES WITH COSMOLOGICAL INFALL

The initial conditions for our simulations are given by the TIS profile for both the gas and the dark-matter density for the virialized halo, with zero bulk velocity, as described by Iliev & Shapiro (2001), and a matching spherical, self-similar infall profile as described by Bertschinger (1985) for the density and infall velocity outside the halo, appropriately generalized to the case of low-density background universe models (Iliev & Shapiro 2001, Appendix A). The match of the post-shock gas in this infall solution to the TIS is discussed in detail in section 7.2 of Shapiro et al. (1999). This match is made possible by the fact that the TIS radius r_t is almost coincident with the shock radius of the self-similar infall solution r_S, with the latter larger than the former by only 1.8 per cent.[4] In order to match the two solutions seamlessly, we continue both the density and the velocity profiles of the infall solution down to r_t. For the velocity profile outside the TIS outer radius we use the pre-shock infall profile of the self-similar solution. Following the notation of Bertschinger (1985), we define the dimensionless radius $\lambda \equiv r/r_{\rm ta}(t)$. Here $r_{\rm ta}$ is the turnaround radius of the shell which is just reaching maximum expansion at time t, whose time dependence is given by $r_{\rm ta}(t) = r_{\rm ta}(t_{\rm i})(t/t_{\rm i})^{8/9}$, where $t_{\rm i}$ is our initial time. Due to self-similarity of the solution every feature in radius occurs at some fixed value of λ. For example, the location of the shock is given by $\lambda_S = 0.338976$, and the time-varying shock radius must follow $r_S(t) = r_{\rm ta}(t)\lambda_S$. Similarly, the radial parameters of the TIS profile, like the core radius r_0 and r_t, follow the same time dependence with $\lambda = (\lambda_0, \lambda_t) = (0.011\,3175, 0.332\,7339)$, respectively.

The physical velocity v at a given radius $r \geqslant r_t$ at time t is given by the following parametric solution

$$\lambda(\theta) = \sin^2\frac{\theta}{2}\left(\frac{\theta - \sin\theta}{\pi}\right)^{-8/9} \tag{A1}$$

and

$$v = \frac{r}{t}\frac{\sin\theta(\theta - \sin\theta)}{(1-\cos\theta)^2} = \frac{r_0(t)}{\lambda_0 t}V(\lambda), \tag{A2}$$

where $0 \leqslant \theta \leqslant 2\pi$. For the TIS density profile we use the fitting formula to the exact numerical results given in Appendix B of Iliev & Shapiro (2001). The resulting initial condition for our simulations is shown in Fig. 4.

In order to evolve the initial dark-matter profile with time self-consistently, we assume that the mass of the TIS grows over time as a result of the infall, and our initial solution for the TIS gives way

[4] In this appendix, spherical symmetry applies throughout, so we use the variable r to mean the spherical radius here.

to a sequence of equilibrium TIS models, where the TIS is specified at each time by the total mass $M(t)$ and redshift $z_{\rm coll}$ at that time. Below we give the time-dependences of all relevant quantities.

The time-dependence of $M(t)$ corresponds to that of the sphere bounded by the accretion shock in the Bertschinger solution. The central density ρ_0 of our TIS solution is just proportional to the mean background density at the same epoch. At the early times of interest to us here, this dependence is simply $\rho_0(t) = \rho_0(t_{\rm i})(t/t_{\rm i})^{-2}$. With this scaling we can write the growth of the total mass with time as

$$M_{\rm TIS}(t) = M_{\rm TIS}(t_{\rm i}) \left[\frac{r_{\rm ta}^3(t)}{r_{\rm ta}^3(t_{\rm i})}\right] \left[\frac{\rho_{\rm b}(t)}{\rho_{\rm b}(t_{\rm i})}\right] = M_{\rm TIS}(t_{\rm i}) \left(\frac{t}{t_{\rm i}}\right)^{2/3}. \quad \text{(A3)}$$

In fact, for any radius which grows in time self-similarly (i.e. keeping its λ-value constant) the mass interior to this radius must grow according to

$$m(\lambda, t) = m(\lambda, t_{\rm i}) \left(\frac{t}{t_{\rm i}}\right)^{2/3}. \quad \text{(A4)}$$

The gravitational acceleration, $a_{\rm grav}$, at radius r of this assumed matter distribution is given simply in terms of the mass $m(r)$ interior to this radius: $a_{\rm grav} = Gm(r)/r^2$. For fixed λ, $m(\lambda, t) \propto t^{2/3}$, so we need only determine $m(r, t) = m[\lambda(r, t), t]$ at fixed r for different times. This is given by

$$m(\lambda, t) = M(\lambda) \frac{4\pi\rho_{\rm b}(t_{\rm i}) r_{\rm S}^3}{3\lambda_{\rm S}^3} \left(\frac{t}{t_{\rm i}}\right)^{2/3}, \quad \text{(A5)}$$

where

$$\lambda(r, t) = \frac{\lambda_0}{r_0(t_{\rm i})} \left(\frac{t}{t_{\rm i}}\right)^{-8/9} r. \quad \text{(A6)}$$

(A) For $\lambda \geqslant \lambda_t = 0.332734$, the infall mass profile is

$$M(\lambda) = -\frac{9}{2}\lambda^2 D(\lambda) \left[V(\lambda) - \frac{8}{9}\lambda\right], \quad \text{(A7)}$$

where $V(\lambda)$ was defined in equation (A2) above and

$$D(\lambda) = \frac{9(\theta - \sin\theta)^2}{16\sin^6(\theta/2)\{1 + 3[1 - 3V(\lambda)/(2\lambda)]\}} \quad \text{(A8)}$$

(Bertschinger 1985).

(B) For $\lambda \leqslant \lambda_t$, the TIS total mass profile is derived by enforcing hydrostatic equilibrium inside the TIS, using the density-profile fitting formula and the isothermal virial temperature to solve for the gravitational acceleration needed to balance the pressure force:

$$M(\lambda) = 6\lambda_0 \left(\frac{\rho_0}{\rho_{\rm b}}\right) \lambda^2 \frac{\zeta[A/(a^2 + \zeta^2)^2 - B/(b^2 + \zeta^2)^2]}{[A/(a^2 + \zeta^2) - B/(b^2 + \zeta^2)]}, \quad \text{(A9)}$$

where $(A, a^2, B, b^2) = (21.38, 9.08, 19.81, 14.62)$, $\zeta = r/r_0$, r_0 is the TIS core radius, and $\rho_{\rm b}$ is the mean background density.

This paper has been typeset from a TEX/LATEX file prepared by the author.